Aromatic spacer engineering for 2D halide perovskites and their application in solar cells

Yi Shen [a], Siliang Hu [a], You Meng [a], SenPo Yip [b], Johnny C. Ho [a,b,c,*]

[a] Department of Materials Science and Engineering, City University of Hong Kong, Kowloon 999077, Hong Kong SAR, PR China
[b] Institute for Materials Chemistry and Engineering, Kyushu University, Fukuoka 816-8580, Japan
[c] State Key Laboratory of Terahertz and Millimeter Waves, City University of Hong Kong, Kowloon 999077, Hong Kong SAR, PR China

ARTICLE INFO

ABSTRACT

Perovskites have emerged as a promising new generation of photovoltaic conversion materials, gradually surpassing traditional silicon-based materials in solar cell research. This development is primarily due to their superior power-conversion efficiency (PCE), simple fabrication process, and cost-effective production. However, the low stability of perovskite ionic crystals poses a significant challenge to their stability, hindering the progress of perovskite materials and devices. Although two-dimensional (2D) perovskites offer improved stability, adding organic amine ions results in a quantum confinement effect that reduces the optoelectronic performance of devices. To counter this issue, the strategic design of suitable spacer cations offers a potential solution. Aromatic amine ions possess greater polarity and structural adjustability compared to aliphatic amine ions, making them advantageous in mitigating the quantum confinement effect. This review focuses on phenylethylammonium (PEA) as a representative aromatic spacer cation. It categorizes the evolution of these cations into four trajectories: alkyl chain modification, substitution of hydrogen atoms on the aromatic ring with specific substituents, replacement of benzene rings with aromatic heterocycles, and utilization of multiple aromatic rings instead of a monoaromatic ring. The structure, properties, and corresponding device performance of aromatic spacer cations utilized in reported 2D perovskites are discussed, followed by the presentation of a series of factors for selecting and designing aromatic amine ions for future development.

1. Introduction

Global climate change is one of the key issues threatening life on earth, which has increasingly attracted the attention of scientists and politicians [1]. Fossil fuels, namely coal, oil, and natural gas, have been identified as the primary contributors to global climate change. Such fuels account for more than 75 % of the total global emissions of greenhouse gases and nearly 90 % of all carbon dioxide emissions. The greenhouse gases emitted by these fuels envelop the earth, trapping the sun's heat and resulting in global warming and climate change. As the energy crisis and environmental damage endanger our planet, developing and utilizing renewable energy sources have become increasingly important. Solar energy, recognized as a highly sustainable source of clean energy, has witnessed a rapid acceleration in its development and utilization. At present, the solar cells available on the market are predominantly silicon-based. However, those silicon cells are characterized by significant defects and impurities, and it has proven difficult to

improve their photoelectric conversion efficiency further. As a result, developing a new generation of solar cells has become an urgent priority [2].

Three-dimensional (3D) organic-inorganic halide perovskite solar cells (PSCs) are widely regarded as the most promising photovoltaic devices currently being developed [3-6]. Over the past decade, PSCs have evolved significantly in terms of PCE [7-12]. Several key features of 3D perovskites contribute to their impressive power conversion efficiency. These include efficient carrier transport [13-15], high absorption coefficient [16-19], high defect tolerance [20], low trap density [8], ambipolar nature [21], and ease of solution processing [22-24]. Perovskites offer potentially higher efficiency than traditional silicon-based materials, simpler manufacturing processes, and reduced costs, making them promising for large-scale commercial applications. However, due to the low decomposition energy of the perovskite material itself, the ions are easy to diffuse and decompose into various sub-phases [25, 26]. When moisture infiltrates the grain boundaries of the perovskite

thin film, it can lead to the degradation of the perovskite structure [27, 28]. This low stability seriously hinders the future commercialization of perovskites. To overcome this issue, various strategies such as interface engineering [29-32], doping [33-35], and encapsulation [36-39] have been attempted. While these methods have successfully modified the properties of perovskite materials, they cannot fundamentally alter its inherent structure. As a result, the potential for enhancing stability remained limited. Fortunately, recent studies have shown that introducing large-volume hydrophobic organic amine ions can significantly enhance the stability of 3D perovskites by cleaving their structure along crystallographic planes forming 2D sheet structures as shown in Fig. 1a [40-43]. Notably, when the introduction of organic cation improves the moisture stability of perovskite, the heat stability, light stability and phase stability can also get a significant enhancement. Besides, unlike traditional 3D perovskites, 2D perovskites possess structural diversity. This diversity results because various organic synthesis methods can be utilized to obtain and study a large variety of organic ammonium ions [44-48]. Consequently, the choice of organic ammonium ions lends a high degree of flexibility in tuning the photoelectric characteristics of 2D perovskites. Additionally, manipulating the number of inorganic layers can result in different optoelectronic properties.

The most common structure of 3D perovskites can be represented by the general formula AMX_3[A = Cs^+, $CH_3NH_3^+$ (MA); M = Pb^{2+}, Ge^{2+}, Sn^{2+}; X = Cl^-, Br^-, I^-]. In terms of 2D perovskites, we mainly have the Ruddlesden-Popper (RP) phase, Dion-Jacobson (DJ) phase and Alternating-Cation-Interlayer (ACI) phase (Fig. 1b). The ACI phase is less studied and can only be constructed using guanidinium. Therefore, we will focus on the RP and DJ phases here. The RP phase has the formula $R_2A_{n-1}M_nX_{3n+1}$, while the DJ phase is represented by $R'A_{n-1}M_nX_{3n+1}$ (n denotes the number of layers of continuous inorganic octahedra between adjacent organic layers). Here, R refers to a bulky organic monoammonium spacer cation, while R' represents a bulky organic diammonium spacer cation. The ideal structure of 2D perovskites is characterized by a systematic and regular alternating of layers containing organic ammonium ions and octahedral layers with a specific number of continuous octahedral layers. In general, obtaining the phase with $n = 1$, which signifies pure 2D perovskites, is relatively straightforward. Nevertheless, preparing a pure phase of quasi-2D perovskites with high n values (ranging from 2 to ∞) is challenging since different n phases have similar crystallization energy. As a result, quasi-2D perovskites often contain multiple n phases, and the nominal n values generally represent the stoichiometry of different compositions in the precursor solutions. In 2D RP perovskites, the organic and inorganic layers are interconnected through hydrogen bonding, while van der Waals forces bind the two ammonium ion layers within the organic layer. Due to the tilt of the Pb - I octahedra, there is a fixed displacement between the inorganic layers in 2D RP perovskites. On the other hand, in 2D DJ perovskites, each diammonium ion can form hydrogen bonds with adjacent octahedral layers on both sides, and no van der Waals effect exists. The linearity of diamine cations in 2D DJ perovskites results in no lateral displacement between neighboring inorganic layers.

Although the stability of 2D perovskites has a great improvement, the PCE still cannot be comparable to 3D perovskite. This is due to the appearance of Quantum Wells (QWs) which is caused by the quantum and dielectric confinement effects, leading to the poor charge transport ability and diffusion length [49,50]. As Fig. 1c shown, the organic layers
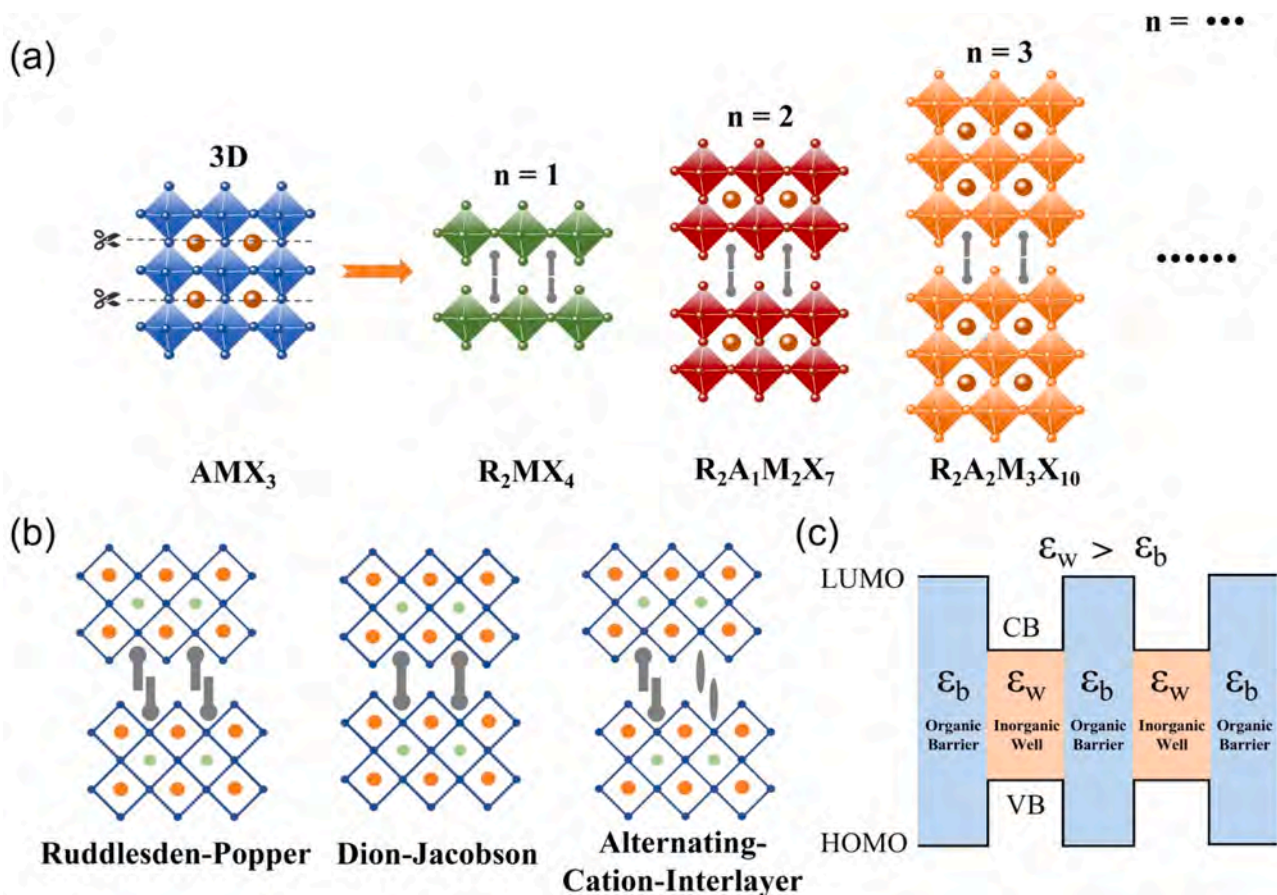

Fig. 1. (a) Structure schematic of 3D and 2D perovskites with n values of 1, 2, and 3, respectively. (b) Schematic of Ruddlesden-Popper (RP), Dion-Jacobson (DJ) and Alternating-Cation-Interlayer (ACI) perovskite structures. (c) Quantum Well schematic of the 2D perovskite where organic layers act as barriers and inorganic layers act as walls. (ε_w represents the dielectric constant of inorganic layers; ε_b represents the dielectric constant of organic layers; LUMO: lowest unoccupied molecular orbital; HOMO: highest occupied molecular orbital; CB: conduction band; VB: valence band).

act as the potential "barriers" and inorganic layers serve as the potential "wells". To be specific, the quantum confinement effect can result in the significant promotion of exciton binding energy (E_b) and the mismatch between dielectric constants of organic layers and inorganic layers also leads to the increase of E_b. This high E_b causes that photo-generated carriers primarily exist as excitons rather than free electrons and holes and to be confined in the QWs, which finally inducing the energy losses. Also, the transport of carriers is hindered by these multiple QWs and mainly occurs through the inorganic sheets. Therefore, improving carrier transport capability between the inorganic and organic layers is crucial for enhancing the electrical performance of 2D perovskite materials. This challenge can potentially be addressed by the reasonable design of new organic ammonium ions. Hence, a comprehensive review and summary of all previously studied ammonium ions is paramount. This knowledge from such a review could pave the way for innovative ideas in future designs.

In both RP and DJ types of 2D perovskites, the spacer ammonium ions can be categorized as aliphatic or aromatic ammonium ions. Some examples of aliphatic ammonium ions for RP perovskites include propylammonium (PA) [51], butylammonium (BA) [52,53], isobutylammonium (IBA) [54-56], while examples of aromatic ammonium ions for 2D RP perovskites include phenylethylammonium (PEA) [57] and 2-thio-phenemethylammonium (TMA) [58]. For 2D DJ perovskites, examples of spacer ammonium ions are propyldiammonium (PDA) [59], butyldiammonium (BDA) [60], and 1,4-phenylenedimethanammonium (PDMA) [61], among others. In recent studies on the development of spacer cations, aromatic spacers have garnered significant attention. In Fig. 2, we show the representative aromatic spacers of RP and DJ perovskites. The complete PCE and stability summaries of common RP and DJ perovskite solar cells are shown in Table 1. It is important to note that compared to aliphatic spacers, aromatic spacers primarily possess the following advantages: (a) Aromatic spacers generally exhibit a larger dielectric constant due to their high dipole moment. This high dielectric constant is favorable for reducing the quantum confinement effect between organic and inorganic layers, enhancing interlayer carrier transfer capability. (b) Aromatic spacers have demonstrated the ability to induce the perpendicular growth of the perovskite lattice, facilitating efficient electron and hole transfer between the substrate and film surface. (c) The inherent structural rigidity and bulk volume of aromatic amine ions, in contrast to aliphatic chain amine ions, effectively limit slippage between the organic layers of 2D perovskites, thus enhancing overall stability. (d) Aromatic molecules offer diverse structural possibilities and can be finely tuned through various chemical synthesis methods. This includes heteroatom substitution of alkyl chains or hydrogen on the aromatic ring and the utilization of aromatic heterocycles. These structural adjustments can lead to tailored properties of 2D perovskites, enabling researchers to obtain perovskite materials with specific characteristics for various applications. Considering the immense potential for further exploration, it becomes paramount to retrospectively evaluate the reported species and characteristics of aromatic amine ions and their impact on the performance of 2D perovskites. This retrospective analysis will provide invaluable guidance for the future development of aromatic spacer cations.

This comprehensive review provides a meticulous overview of research conducted on aromatic spacer cations in 2D perovskites. Our primary focus emphasizes the intrinsic properties of these aromatic spacers, including volume, hydrophobicity, dipole moment, and so on, as well as their influence on the performance of 2D perovskites. These properties influence various aspects, such as the distribution patterns of different n-phases, grain growth direction, distortion degree of inorganic PbI_6 octahedra, and stacking mode of organic amine ions. Additionally, we explore the implications of these factors on device efficiency and stability. Eventually, we underscore a set of factors for selecting and designing aromatic amine ions while speculating on potential avenues for future research.

2. Aromatic monoamine spacer cations of 2D RP perovskites

2D RP perovskites have attracted considerable research interest in recent years, with a significant growth in the diversity of aromatic monoamine cations applied in 2D RP perovskites. Structurally, in 2D RP perovskites, the amino end of the monoamine cation is tethered to the inorganic octahedral layer via hydrogen bonds. In contrast, the opposing end is linked to amine ions through van der Waals interactions. Notably, various aromatic monoamine ions can be viewed as derivatives of PEA which was firstly reported in 2014 [41], following four distinct pathways: modification of alkyl chains, replacement of hydrogen atoms on the aromatic ring with specific substituents, substitution of benzene rings with aromatic heterocycles, and replacement of a monoaromatic ring with polyaromatic rings. This summary will summarize the different types of aromatic monoamine ions and their applications in 2D RP perovskites, considering these four aspects.

2.1. Modification of alkyl chains

The modification of alkyl chains in aromatic spacer amine ions has a significant impact on the performance of 2D RP perovskites. However, the related research is limited. The primary modifications of alkyl chains include adjusting the length of the alkyl chain, incorporating conjugated double bonds, and introducing heteroatoms.

Kamminga et al. studied 2D RP perovskite single crystals using phenylalkylammonium cations [57]. These cations had varying numbers of carbon atoms between the phenyl ring and amino group, namely PMA (1), PEA (2), PPA (3), and PBA (4) (Fig. 3a-c). The research findings revealed an interesting trend in the photoluminescence (PL) spectrum as the carbon chain length increased from 1 to 4 (Fig. 3c). Specifically, there was a noticeable blue-shift in the PL peak. Upon analyzing the single crystal structures, it was observed that compounds corresponding to PMA and PEA, which had shorter ligand lengths, exhibited an inorganic structure composed of corner-sharing PbI_6 octahedra (Fig. 3a, b). As the alkyl chain length increased, the Pb-I-Pb bond angle also increased, indicating a larger distortion in the PbI_6 octahedra sheet. On the other hand, the two compounds with longer alkyl chains, PPA and PBA, showed a different connection mode with both corner- and face-sharing PbI_6 octahedra sheets (Fig. 3a, b). The electronic structures were calculated using density functional theory (DFT), and the results indicated that the increase in spacer cation length led to systematic changes in the energy band structure. This observation was consistent with the structural changes from 3D to 2D and 1D with face-sharing PbI_6-octahedra.

In 2020, Wu et al. achieved a significant breakthrough by incorporating a unique aromatic amine molecule with a double bond in the alkyl chain (3-phenyl-2-propen ammonium or PPeA (6)) as a spacer in 2D RP perovskites [92]. This development led to the successful synthesis of a single crystal structure denoted as $(PPeA)_2(FA_{0.5}MA_{0.5})_{n-1}Pb_nI_{3n+1}$ (where n = 2, 3, 4) (Fig. 3d). Through analysis of the single crystal structure, it was observed that the presence of sp^2 hybridization in the -CH=CH- group allowed for the formation of multiple hydrogen bonds between the halide ions of the PbI_6 octahedra and the spacer cations, facilitating deeper penetration of organic spacers. Therefore, the perovskite structure with alternating organic layers and inorganic layers was effectively stabilized. Moreover, the network of hydrogen bonds between PPeA and the PbI_6 octahedra played a crucial role in linking adjacent inorganic layers, thus inhibiting in-plane crystal growth of the 2D RP perovskite films. As a result of incorporating the PPeA spacer into the 2D RP perovskite structure, an outstanding PCE of 14.76 % was achieved for the composition with n = 4. Furthermore, these perovskite devices exhibited excellent stability under high temperature and humidity conditions, highlighting their potential for practical applications.
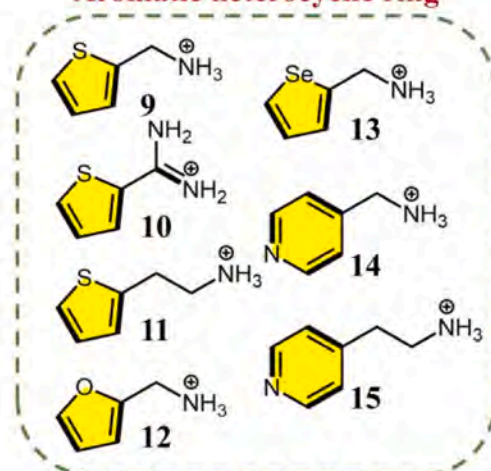
Derived from primary amines, the secondary, tertiary and quaternary amines were also studied in perovskites [65,93-95]. Jesus et al. figured out that with the increase of the number of substitution located

Aromatic monoamine cations
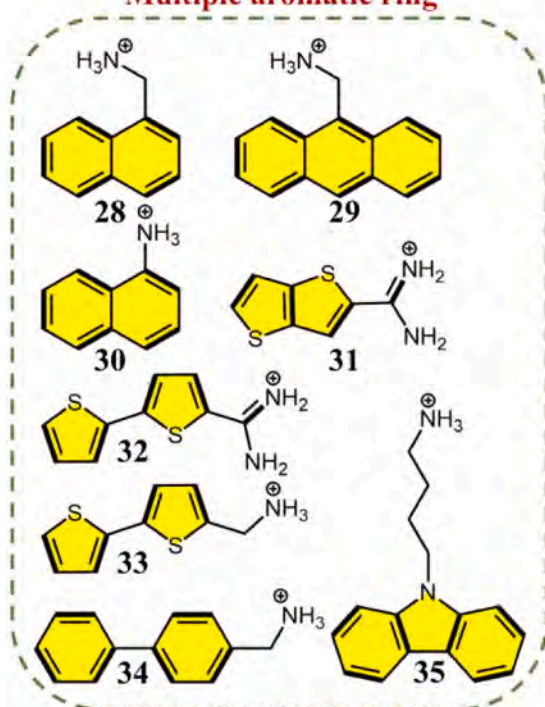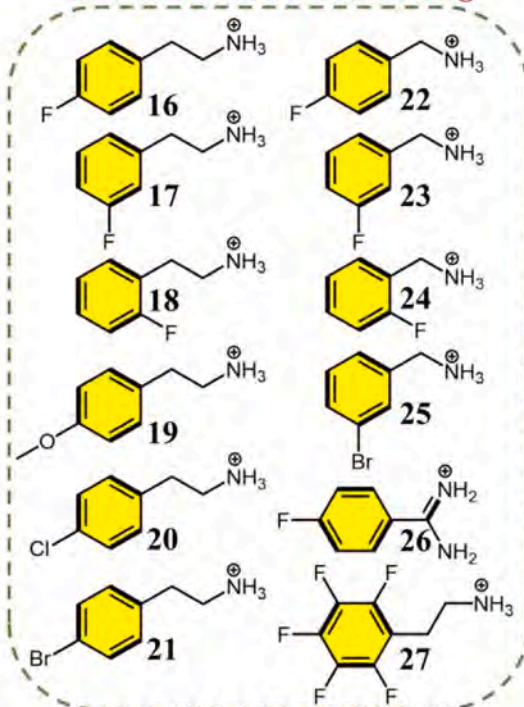
Modification of alkyl chains
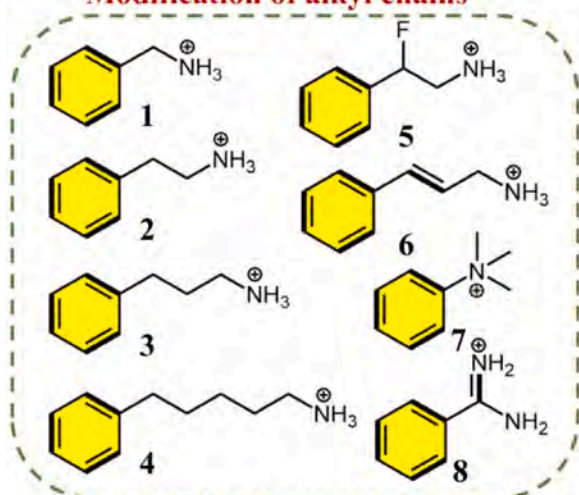
Aromatic heterocyclic ring
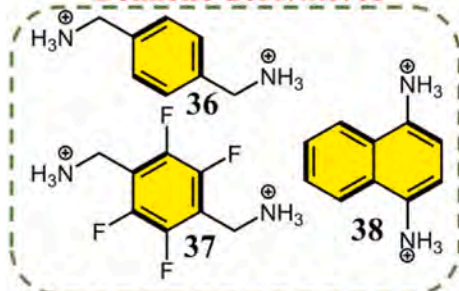
Multiple aromatic ring
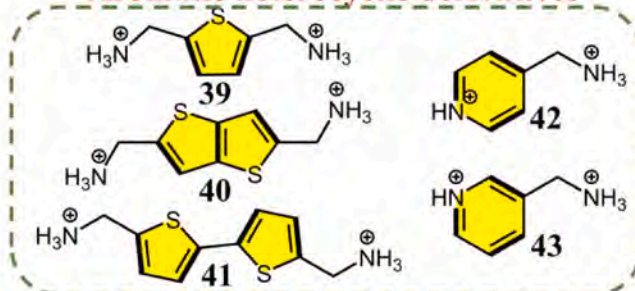
Substitution on aromatic ring

Aromatic diamine cations

Benzene derivatives

Aromatic heterocyclic derivatives

(caption on next page)

Fig. 2. Aromatic monoamine and diamine cations. Aromatic monoamine cations: **1**, Benzylammonium (PMA) **2**, Phenylethylammonium (PEA) **3**, 3-phenyl-1-propylammonium (PPA) **4**, 4-Phenyl-1-butylammonium (PBA) **5**, 2-Fluoro-2-phenylethan-1-aminium (β-FPEA) **6**, 3-Phenyl-2-propenammonium (PPeA) **7**, Phenyl-trimethylammonium (PTA) **8**, Benzamidine (PhFA) **9**, 2-Thiophenemethylammonium (TMA) **10**, 2-Thiopheneformamidinium (ThFA) **11**, 2-Thiophene ethyl-ammonium (TEA) **12**, 2-Furfurylammonium (FuMA) **13**, 2-Selenophenemethylammonium (SeMA) **14**, 4-(Aminoethyl)pyridine (4-AEP) **15**, 4-Pyridinylmethylammonium (PyA) **16**, 4-Fluoro-phenethylammonium (4F-PEA/pF1PEA) **17**, 3-Fluoro-phenethylammonium (mF1PEA) **18**, 2-Fluoro-phenethylammonium (oF1PEA) **19**, 4-Methoxyphenethylammonium (MeO-PEA) **20**, 4-Chloro-phenylethylammonium(4Cl-PEA) **21**, 4-Bromo-phenylethylammonium (4Br-PEA) **22**, 4-Fluoro-benzylammonium (pFBA) **23**, 3-Fluoro-benzylammonium (mFBA) **24**, 2-Fluoro-benzylammonium (oFBA) **25**, 3-bromobenzylammonium (3BBA) **26**, 4-Flu-oro-benzamidine (p-FPhFA) **27**, 2,3,4,5,6-pentaFluoro-phenethylammonium (F5-PEA) **28**, 1-Naphthalenemethylammonium (NpMA) **29**, 9-Anthracenemethylammonium (AnMA) **30**, 1-Naphthylamine (1-NA) **31**, amino(thieno[3,2-b]thiophen-2-yl)methaniminium (TTFA) **32**, [2,2′-bithiophen]−5-yl(amino)methaniminium (BTFA) **33**, Bithiophenemethylammonium (BThMA) **34**, Biphenemethylammonium (BPhMA) **35**, (9H-carbazol9-yl)butyl-1-ammonium (CA) **Aromatic diamine cations: 36**, 1,4-Phenylenedimethanam-monium (PDMA) **37**, 2,3,5,6-Tetrafluoro-1,4-benzenedimethanammonium (TFBDA) **38**, 1,5-diaminonaphthalene (NDA) **39,** 2,5-thiophenedimethylammonium (ThDMA) **40**, Thieno[3,2-b]thiophene-2,5-diyldimethanaminium (TTDMA) **41**, Bithiophene dimethylammonium (BThDMA) **42**, 3-(aminomethyl)pyridinium (3AMPY) **43**, 4-(aminomethyl)pyridinium (4AMPY).

on the amino group, the effective interaction between organic spacers and octahedral sheets may be weakened owing to the reduction of hydrogen bonds and increase of steric hindrance. In Chen's work, they successfully used phenyl-based primary (PA), secondary (NPA), tertiary (DPA) and quaternary ammonium (PDA)(7) to prepare 2D perovskites with $n = 4$, which show PCEs of 3.9 %, 7.8 %, 4.3 % and 11.53 % in solar cell devices, respectively. The higher PCE of PDA-based PSC was ascribed to its high-quality film, low defects and suitable energy levels.

Fluorination is a common strategy to augment the performance of 2D perovskite devices. Still, most related research has primarily focused on substituting fluorine into the benzene ring of aromatic amines. Due to the complexity and difficulty of the synthetic route, only limited research has been conducted on fluorine substitution on the alkyl chain of aromatic amines. Recently, Zhang et al. synthesized a new aromatic spacer cation called β-FPEA (5), which introduced a fluorine substituent on the first carbon atom of the alkyl chain in PEA [78]. DFT calculations revealed that β-FPEA possessed a dipole moment of 1.71 Debye, greater than that of PEA (1.26 Debye) (Fig. 3e). The higher polarity was bene-ficial to facilitate exciton dissociation and charge transport. Moreover, the presence of fluorine atoms of β-FPEA resulted in positive charge accumulation on NH_3^+ due to its strong electron-pulling capability. This fact leads to enhanced interaction between β-FPEA spacers and inor-ganic octahedral layers. By combining β-FPEA cations with FA cations, the researchers prepared 2D perovskite films of (β-FPEA)$_2$(FA)$_{n−1}$Pb$_n$I$_{3n+1}$ and (PEA)$_2$(FA)$_{n−1}$Pb$_n$I$_{3n+1}$ (n = 5) via a simple spin-coating process. X-ray photoelectron spectroscopy (XPS) measurements indicated a shift of approximately 0.1 eV towards lower binding energy in the Pb and I peaks of β-FPEA-based 2D perovskite films compared to PEA-based films, reflecting a change in the chemical environment of Pb and I atoms (Fig. 3f). Scanning electron microscopy (SEM) revealed that the crystals in β-FPEA-based 2D perovskite films exhibited a sheet-like shape with a vertical growth direction relative to the substrate. In contrast, PEA-based 2D perovskite films displayed needle-shaped crystals parallel to the substrate, accompanied by larger grain boundaries. X-ray diffraction (XRD) and grazing-incidence wide-angle X-ray scattering (GIWAXS) measurements demonstrated that PEA-based 2D perovskite films possessed (0k0) diffraction peaks representative of a lower n phase, whereas the (111) diffraction peaks of β-FPEA-based 2D perovskite films were notably stronger (Fig. 3g). These differences indicated that introducing a fluorine atom on the alkyl chain improves the crystallinity of 2D perovskites and promotes crystal growth perpendicular to the substrate. Time-resolved PL measurements showed that after 10 min, the PL peak of PEA-based 2D perovskite films shifted towards shorter wavelengths, accompanied by the appearance of new emission peaks associated with the low n phase. However, β-FPEA-based 2D perovskite films exhibited nearly unchanged spectra in PL mapping. Time-resolved XRD tests yielded consistent results, further indicating the improved stability of β-FPEA-based 2D perovskite films. Finally, performance studies of PSCs based on PEA and β-FPEA revealed that introducing fluorine on the alkyl chain of PEA led to an enhanced PCE from 12.81 % to 16.77 %. Additionally, when devices were prepared on the PTAA substrate, a higher PCE of 19.11 % was achieved. This

improvement in device performance can be attributed to the increased carrier diffusion length and lifetime and decreased trap density in β-FPEA-based 2D perovskites. This work pioneered a new way of pro-moting the performance and stability of 2D RP perovskite devices by introducing substituents to modify the alkyl chain of aromatic amines.

2.2. Aromatic heterocyclic ring

Aromatic heterocyclic ring spacers have great application potential in 2D RP perovskites. Specially, the thiophene ring has garnered sig-nificant attention due to its promising properties in various fields, such as organic chemistry, organic semiconductor materials, electron-transporting materials, and hole-transporting materials. Incorporating thiophene rings and their derivatives in 2D RP perovskites is believed to regulate the energy band arrangement [58,64,70,96-101]. Furthermore, the presence of S atoms strengthens the interaction between inorganic and spacer cations layers, thereby contributing to stabilizing the 2D perovskite lattices [64]. Additionally, researchers have extensively explored other heteroaromatic rings such as furan [74,102], seleno-phene [72], and pyridine [66,68,83,103-106] for their potential to be introduced into the spacer cations layers of 2D RP perovskites.

In 2018, Chen et al. successfully incorporated the thiophene ring into 2D RP perovskites [58]. They introduced a thiophene-based spacer cation known as 2-thiophenemethylammonium (ThMA)(9) and syn-thesized (ThMA)$_2$(MA)$_{n−1}$Pb$_n$I$_{3n+1}$ (n = 3) perovskite films. Adding MACl additives aided in achieving a nanorod-like structure for the perovskite films (Fig. 4a). By adjusting the weight ratio of MACl/MAI between 0 and 1, the researchers discovered that a ratio of 0.5 yielded perovskite films with superior crystallinity and an ordered structure, as depicted in Fig. 4a. Furthermore, at this optimal weight ratio, the perovskite films exhibited a preferential growth direction perpendicular to the substrate, which was advantageous for charge transport. The fabricated PSCs device utilizing (ThMA)$_2$(MA)$_{n−1}$Pb$_n$I$_{3n+1}$ (n = 3) perovskite films demonstrated an impressive PCE of 15.42 %.

Formamidinium (FA) is a crucial cation that can substitute the MA cation in the 3D perovskite lattice. Liu and colleagues incorporated the ThMA spacer cation into the FAPbI$_3$ perovskite system, resulting in the formation of n = 3 perovskite films, namely (ThMA)$_2$(FA)$_2$Pb$_3$I$_{10}$ [96]. Compared to MA-based (ThMA)$_2$(MA)$_2$Pb$_3$I$_{10}$ PSCs, the introduction of FA cation in the devices increased PCE from 15.42 % to 16.18 %. This improvement can be attributed to the FA cation's ability to narrow the band gaps. A crystal growth technique assisted by the use of 4-(tri-fluoromethyl) benzyl ammonium iodide was employed in this study to enhance perovskite crystallinity, minimize trap density, and reduce nonradiative recombination losses. The high-resolution transmission electron microscopy (HRTEM) and GIWAXS characterization revealed the presence of low n values, high n values, and 3D phase in the 2D perovskite films. As a result, the final PCE of the optimized devices displayed a significant enhancement, reaching up to 19.06 %.

2-Thiophene ethylamine (TEA) (11) is an organic spacer cation with a longer alkyl chain than TMA. A study by Liang et al. utilized TEA as a spacer cation in synthesizing 2D RP perovskite films, with PEA as a

Table 1
The summaries of representative PCE and stability for common RP and DJ perovskite solar cells.

Device structure	2D Perovskite	PCE (%)	Stability	Ref
FTO/c-TiO$_2$/perovskite/spiroOMeTAD/Au	(PEA)$_2$(MA)$_2$Pb$_3$I$_{10}$	4.73	NA	[41]
ITO/PTAA/perovskite/PCBM/PEI/Ag	(PEA)$_2$MA$_4$Pb$_5$I$_{16}$	11.10	70 % retained after 500 h (Air, 60 % RH, without encapsulation)	[62]
			65 % retained after 500 h (N$_2$, 55 °C, without encapsulation)	
ITO/PEDOT:PSS//perovskite/PCBM/BCP/Ag	(PEA)$_2$(MA)$_4$Pb$_5$I$_{16}$	14.10	90 % retained after 1080 h (Air, 30 % RH, with encapsulation)	[63]
ITO/PEDOT:PSS/perovskite/PCBM/Bphen/Al	(TEA)$_2$(MA)$_4$Pb$_5$I$_{16}$	7.20	80 % retained after 270 h (Air, 60 % RH, 25 °C, without encapsulation)	[64]
ITO/SnO$_2$/perovskite/spiroOMeTAD/Ag	(PTA)$_2$(MA)$_3$Pb$_4$I$_{13}$	11.53	90 % retained after 1600 h (N$_2$, RT, without encapsulation)	[65]
FTO/C$_{60}$/perovskite/spiroOMeTAD/Au	(4-AEP)$_2$MA$_4$Pb$_5$I$_{16}$	11.68	95 % retained after 1000 h (Air, 30 % RH, RT, without encapsulation)	[66]
ITO/PEDOT:PSS/perovskite/PCBM/BCP/Ag	(PhFA)$_2$MA$_4$Pb$_5$I$_{16-x}$Cl$_x$	12.92	68 % retained after 3000 h (N$_2$, without encapsulation)	[67]
			77 % retained after 450 h (N$_2$, continuous illumination, without encapsulation)	
ITO/PEDOT:PSS/perovskite/spiroOMeTAD/Au	(BA$_{0.9}$PyA$_{0.1}$)$_2$MA$_3$Pb$_4$I$_{13}$	13.01	98 % retained after 1200 h (N$_2$, without encapsulation)	[68]
ITO/PTAA/perovskite/C$_{60}$/BCP/Cu	(PPeA)$_2$(FA$_{0.5}$MA$_{0.5}$)$_3$Pb$_4$I$_{13}$	14.76	94 % retained after 600 h (Air, 85 % RH, 85 °C, with encapsulation)	[69]
ITO/PEDOT:PSS/perovskite/PCBM/BCP/Ag	(ThMA)$_2$(MA)$_2$Pb$_3$I$_{10}$	15.42	90 % retained after 1000 h (N$_2$, without encapsulation)	[58]
ITO/PEDOT:PSS/perovskite/PCBM/BCP/Ag	(ThFA)(Cs)$_4$Pb$_5$I$_{16}$	16.00	92 % retained after 960 h (N$_2$, without encapsulation)	[70]
ITO/PTAA/perovskite/PCBM/BCP/Ag	(pFBA)$_2$(MA)$_4$Pb$_5$I$_{16}$	17.12	100 % retained after 2000 h (Ar, without encapsulation)	[71]
			83 % retained after 600 h (Air, 60 % RH, 25 °C, without encapsulation)	
ITO/PEDOT:PSS/perovskite/PDTL/PCBM/BCP/Ag	(SeMA)$_2$(MA)$_4$Pb$_5$I$_{16}$	17.25	100 % retained after 1008 h (Air, 30 % RH, without encapsulation)	[72]
			86 % retained after 1008 h (N$_2$, 60 °C, without encapsulation)	
			97 % retained after 1008 h (N$_2$, continuous illumination, without encapsulation)	
ITO/PEDOT:PSS/perovskite/PCBM/BCP/Ag	(NpMA)$_2$(MA)$_3$Pb$_4$I$_{13}$	17.25	91 % retained after 4100 h (N$_2$, RT, without encapsulation)	[73]
			89 % retained after 1000 h (Air, 30 ± 5 % RH, without encapsulation)	
			80 % retained after 600 h (N$_2$, 80 °C, without encapsulation)	
			79 % retained after 600 h (N$_2$, continuous illumination, without encapsulation)	
ITO/PEDOT:PSS/perovskite/PCBM/BCP/Ag	(p-FPhFA)$_2$(MA)$_4$Pb$_5$I$_{16}$	17.37	99 % retained after 3000 h (N$_2$, without encapsulation)	[67]
			82 % retained after 450 h (N$_2$, continuous illumination, without encapsulation)	
ITO/PEDOT:PSS/perovskite/PCBM/BCP/Ag	(FuMA)$_2$MA$_3$Pb$_4$I1$_9$Cl$_4$	18.00	94 % retained after 1850 h (N$_2$, without encapsulation)	[74]
			83 % retained after 768 h (N$_2$, 85 °C, without encapsulation)	
			80 % retained after 768 h (N$_2$, continuous illumination, without encapsulation)	
ITO/PTAA/perovskite/PCBM/Cr/Au	3BBA-based perovskite	18.2	82 % retained after 2400 h (Air, 40 % RH, RT, without encapsulation)	[75]
ITO/TiO$_2$/perovskite/Spiro-OMeTAD/Au	(CA)$_2$(MA)$_4$Pb$_5$I$_{16}$	18.23	85 % retained after 2000 h (Air, 65 % RH, 25 °C, without encapsulation)	[76]
ITO/PEDOT:PSS/Perovskite/PCBM/BCP/Ag	(BThMA)$_2$(MA)$_4$Pb$_5$I$_{16}$	18.85	89 % retained after 670 h (Air, 45 % RH, without encapsulation)	[77]
ITO/PTAA/perovskite/PCBM/BCP/Ag	(β-PEA)$_2$(MA)$_4$Pb$_5$I$_{16}$	19.11	90 % retained after 720 h (70 °C, without encapsulation)	[78]
			86 % retained after 780 h (Air, 35 % RH, without encapsulation)	
ITO/PEDOT:PSS/perovskite/PCBM/BCP/ Ag	(BTFA)$_2$(MA)$_4$Pb$_5$I$_{16}$	15.43	78 % retained after 777 h (N$_2$, continuous illumination, without encapsulation)	[79]
ITO/PEDOT:PSS/perovskite/PCBM/BCP/ Ag	(TTFA)$_2$(MA)$_4$Pb$_5$I$_{16}$	19.41	90 % retained after 777 h (N$_2$, continuous illumination, without encapsulation)	[79]
FTO/TiO$_2$/perovskite/spiroOMeTAD/Au	(4F-PEA)$_2$(MA)$_4$Pb$_5$I$_{16}$	13.64	65 % retained after 576 h (Air, 75 °C, without encapsulation)	[80]
ITO/PTAA/perovskite/PCBM/PEI/Ag	(4F-PEA)$_2$MA$_4$Pb$_5$I$_{16}$	17.34	93 % retained after 500 h (Air, 60 % RH, without encapsulation)	[62]
			94 % retained after 500 h (N$_2$, 55 °C, without encapsulation)	
ITO/PTAA/perovskite/PCBM/PEI/Ag	(4F-PEA)$_2$(MA)$_3$Pb$_4$I$_{13}$	18.10	90 % retained after 720 h (Air, 45 % RH, without encapsulation)	[81]
			80 % retained after 720 h (N$_2$, 80 °C, without encapsulation)	
ITO/PTAA/perovskite/PCBM/BCP/Ag	(4F-PEA)$_2$(FA)$_4$Pb$_5$I$_{16}$	21.07	97 % retained after 1500 h (N$_2$, 80 °C, without encapsulation)	[82]
			90 % retained after 1200 h (Air, 40 % RH, 25 °C, without encapsulation)	
FTO/cp-TiO$_2$/mp-TiO$_2$/perovskite/ spiroOMeTAD/Au	(PDMA)(FA)$_2$Pb$_3$I$_{10}$	7.00	85 % retained after 60 days (Air, 30−50 % RH, without encapsulation)	[61]
FTO/PEDOT:PSS/perovskite/C$_{60}$/BCP/Ag	(3AMPY)(MA)$_3$Pb$_4$I$_{13}$	9.20	NA	[83]
ITO/PEDOT:PSS/perovskite/PCBM/Bphen/Ag	(PDMA)MA$_5$Pb$_6$I$_{19}$	11.00	NA	[84]
FTO/c-TiO$_2$/perovskite/Spiro-OMeTAD/Au	(PDMA)(MA)$_3$Pb$_4$I$_{13}$	15.81	NA	[85]
FTO/TiO$_2$/SnO$_2$/perovskite/Spiro-OMeTAD/Au	(NDA)(MA)$_3$Pb$_4$I$_{13}$	15.08	75 % retained after 1000 h (Air, 60 % RH, without encapsulation)	[86]
			70 % retained after 200 h (85 °C, without encapsulation)	
ITO/SnO$_2$/perovskite/Spiro-OMeTAD/Au	(TFBDA)(MA)$_9$Pb$_{10}$I$_{31}$	15.24	93 % retained after 1300 h (Air, 40−70 % RH, without encapsulation)	[87]
			80 % retained after 100 h (80 °C, without encapsulation)	
ITO/PEDOT:PSS/perovskite/PCBM/BCP/Ag	(TFBDA)(MA)$_3$Pb$_4$I$_{13}$	16.62	93 % retained after 1839 h (N$_2$, RT, without encapsulation)	[88]
ITO/PEDOT:PSS/perovskite/PCBM/BCP/Ag	(ThDMA)(MA)$_4$Pb$_5$I$_{16}$	15.75	95 % retained after 1655 h (N$_2$, RT, without encapsulation)	[89]
ITO/PEDOT:PSS/Perovskite/PCBM/BCP/Ag	(BThDMA)(MA)$_4$Pb$_5$I$_{16}$	18.10	100 % retained after 3100 h (N$_2$, without encapsulation)	[90]
			100 % retained after 500 h (Air, 30−50 % RH, without encapsulation)	
			82 % retained after 300 h (N$_2$, 85 °C, without encapsulation)	
ITO/PEDOT:PSS/perovskite/PCBM/BCP/Ag	(TTDMA)(MA)$_3$Pb$_4$I$_{13}$	18.82	99 % retained after 4400 h (N$_2$, without encapsulation)	[91]
			94 % retained after 740 h (N$_2$, continuous illumination, without encapsulation)	
			94 % retained after 740 h (N$_2$, 80 °C, without encapsulation)	
			98 % retained after 960 h (Air, 30 % RH, RT, without encapsulation)	

comparative reference [64]. XPS measurements revealed a noticeable trend of decreasing binding energy from MAPbI$_3$ to PEA and TEA, as shown in Fig. 4b. This trend, represented by the change in the characteristic peaks of Pb, confirmed the distinct interaction between S atoms and Pb atoms. This interaction induced electronic coupling between the organic and inorganic layers, stabilizing the lattice structure of inorganic octahedral layers and enhancing exciton dissociation and interphase charge transfer. Moreover, this interaction facilitated the nucleation of the 3D phase at the 2D phase grain boundaries, promoting the formation of 2D/3D heterojunctions (Fig. 4c). The presence of these
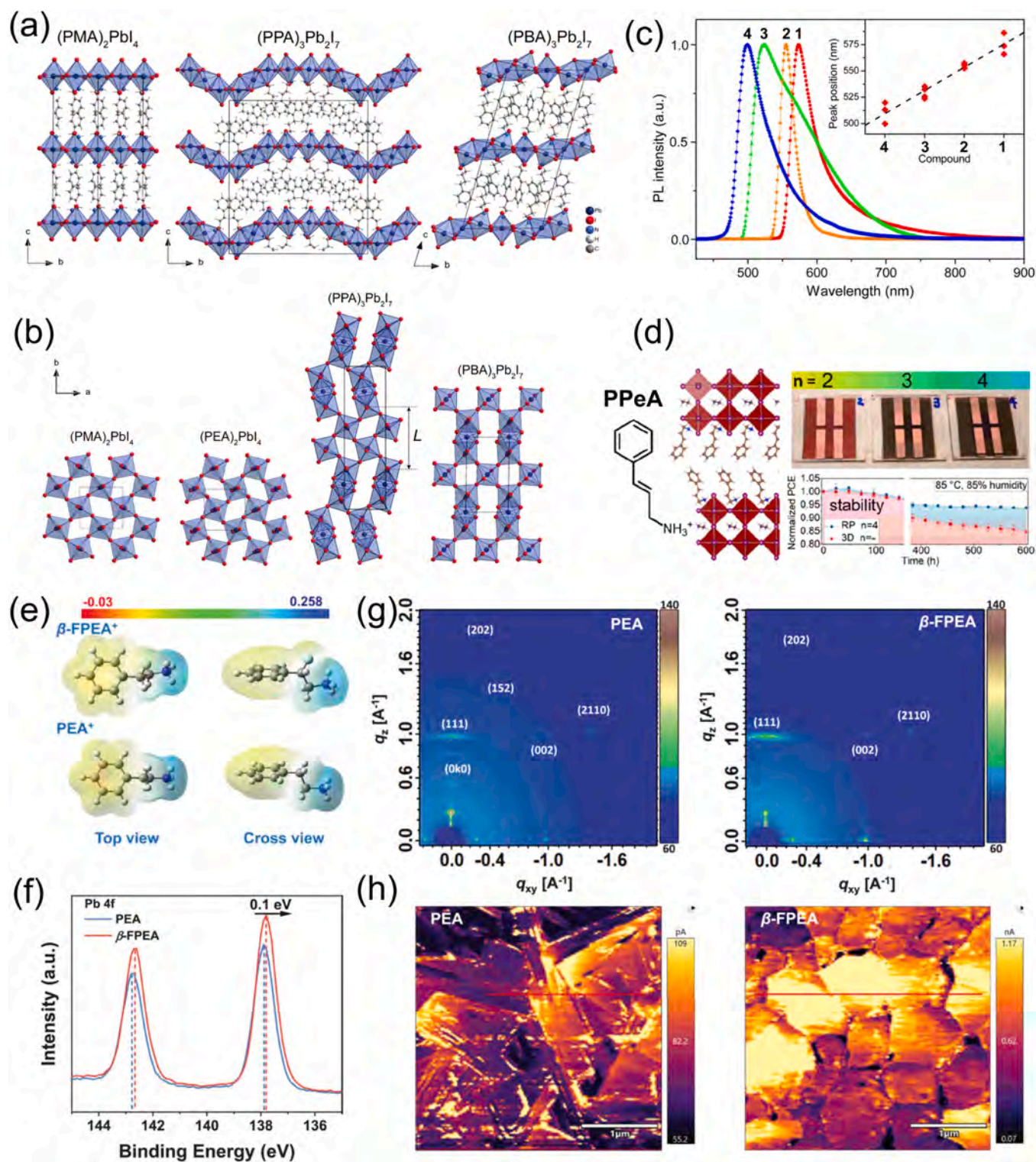
Fig. 3. (a) Single crystal structure of $(PMA)_2PbI_4$, $(PPA)_3Pb_2I_7$, and $(PBA)_3Pb_2I_7$ perovskites at 100 K, projected along the [100] direction. (b) Single crystal structure of $(PMA)_2PbI_4$, $(PEA)_2PbI_4$, $(PPA)_3Pb_2I_7$, and $(PBA)_3Pb_2I_7$, projected along the [001] direction. The organic molecules are not shown for clarity. (c) Selected PL spectra for Compounds $1 - 4$, which are referred to as $(PMA)_2PbI_4$, $(PEA)_2PbI_4$, $(PPA)_3Pb_2I_7$, and $(PBA)_3Pb_2I_7$, respectively. (d) Chemical structure of PPeA and stability measurement of PPeA-based PSCs. (e) Calculated ESP maps for β-FPEA and PEA spacers. (f) XPS spectra of the Pb 4f orbitals of PEA- and β-FPEA based 2D RP perovskite films. (g) GIWAXS results of PEA-based and β-FPEA-based 2D RP perovskite films. (h) AFM images of PEA-based and β-FPEA-based 2D RP perovskite films. (a-c) Reproduced with permission from Ref. [57]. Copyright 2016, American Chemical Society. (d) Reproduced with permission from Ref. [92]. Copyright 2020, American Chemical Society. (e-h) Reproduced with permission from Ref. [78]. Copyright 2023, Wiley-VCH.
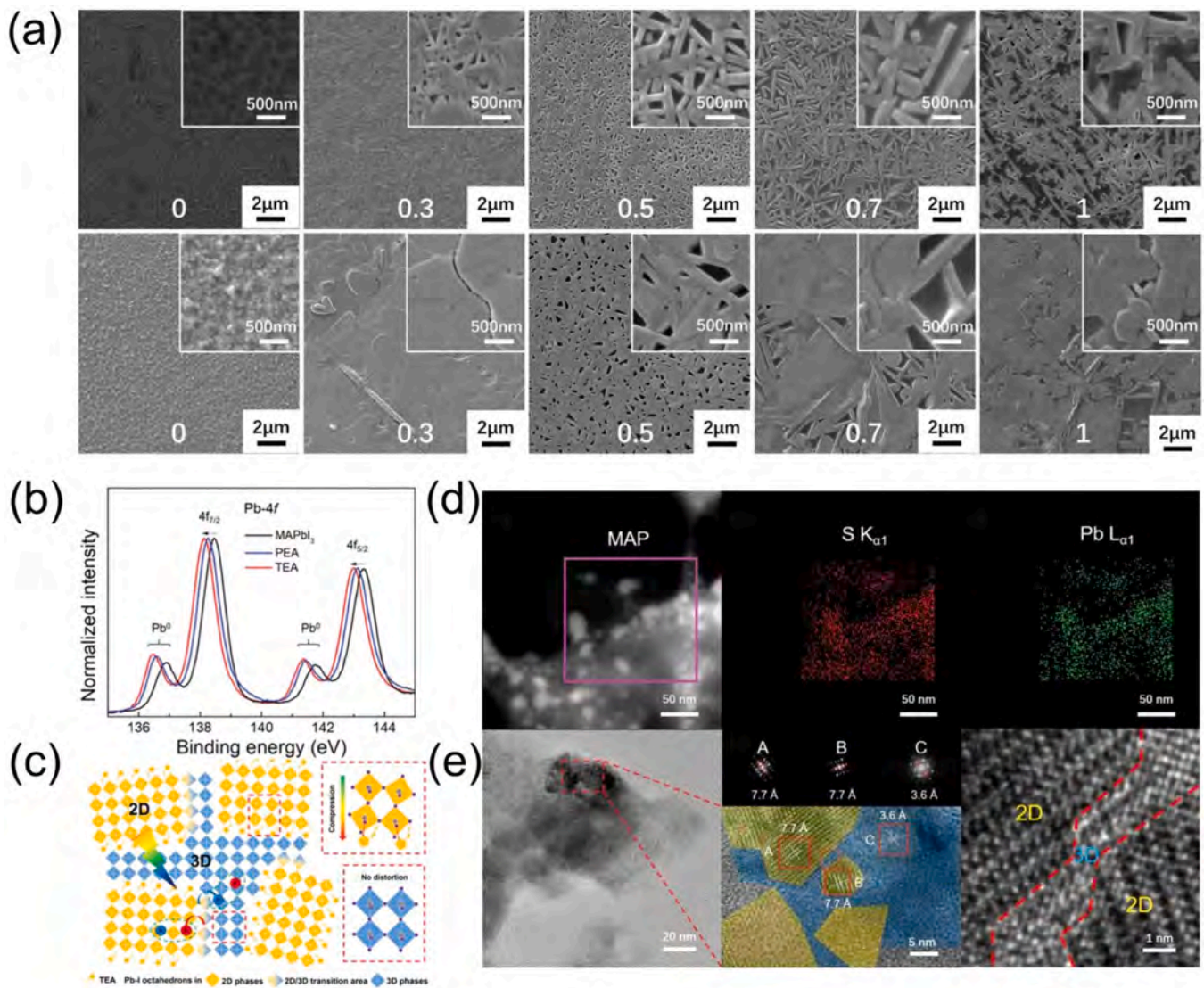
Fig. 4. (a) SEM images of ThMA-based perovskite films with different MACl/MAI weight ratios from 0 to 1 before thermal annealing (top) and after thermal annealing (bottom). (b) XPS spectra of Pb 4f for MAPbI$_3$ perovskite, PEA-based, and TEA-based 2D perovskite thin films, respectively. (c) Schematic illustration of 2D/3D mixed phases in TEA-based 2D RP perovskites. (d) STEM images and corresponding EDS elemental mapping of TEA-based 2D RP perovskites. (e) TEM and magnified HR-TEM image for TEA-based 2D RP perovskites. (a) Reproduced with permission from Ref. [58]. Copyright 2018, American Chemical Society. (b-e) Reproduced with permission from Ref. [64]. Copyright 2019, Wiley-VCH.

heterojunctions was validated by techniques such as TEM and Energy-Dispersive X-ray Spectroscopy (EDS) (Fig. 4d). The formation of 2D/3D heterojunctions extended exciton diffusion length and carrier lifetime, leading to a higher PCE of 11 % in TEA-based 2D PSCs compared to the PEA-based counterpart. Additionally, the TEA-based 2D PSCs demonstrated remarkable phase and device performance stability. In Yao's research, perovskite single crystals ((TEA)$_2$(MA)$_2$Pb$_3$I$_{10}$) based on TEA with $n = 3$ were dissolved in a designated solvent (mixed DMAc: TOL (HI) solvent), yielding a special solution that acted as precursor solution before spin-coating. Importantly, the 2D perovskite films, derived from this precursor solution via the thermal spin-coating method, maintained a consistent primary phase ($n = 3$) analogous to the dissolved single crystal. Compared to PSCs prepared using conventional stoichiometric precursors, the PSCs fabricated through this novel approach achieved a peak PCE of 14.68 % after optimization. This co-ordination engineering provided an important avenue for obtaining high-quality 2D RP perovskite films with a narrow n-phase distribution.

2-Thiopheneformamidinium (ThFA)(10), a fusion of thiophene and FA cation was initially synthesized and employed in 2D RP perovskite

(ThFA)$_2$MA$_2$Pb$_3$I$_{10}$ by Liu et al. in 2020 [96]. They pioneered a Precursor Organic Salts-Assisted Crystal Growth (PACG) methodology to enhance the quality of 2D RP perovskite films. By employing PACG technology, the solar cell devices demonstrated an impressive PCE of 16.72 %. This significant achievement was attributed to the extended carrier lifetime, increased carrier mobility, and reduced nonradiative recombination observed in the ThFA-based 2D RP perovskite films. Building upon their previous work, Liu and colleagues further expanded the application of ThMA and ThFA spacer cations by incorporating them into CsPbI$_3$-based perovskite [70]. This incorporation led to the development of 2D RP perovskite films and PSC devices with an n-value of 5, specifically (ThMA)$_2$Cs$_4$Pb$_5$I$_{16}$ (ThMA-Cs) and (ThFA)$_2$Cs$_4$Pb$_5$I$_{16}$ (ThFA-Cs). SEM images displayed in Fig. 5a revealed that ThFA-Cs perovskite films exhibited superior morphological quality, characterized by enlarged grain sizes. In contrast, ThMA-Cs perovskite films displayed smaller grain sizes and noticeable pinholes. The presence of large, substrate-perpendicular grains in ThFA-Cs films contributed to enhanced carrier transport ability and reduced electron-hole pair recombination. Graphical interpretation of GIWAXS results in Fig. 5b
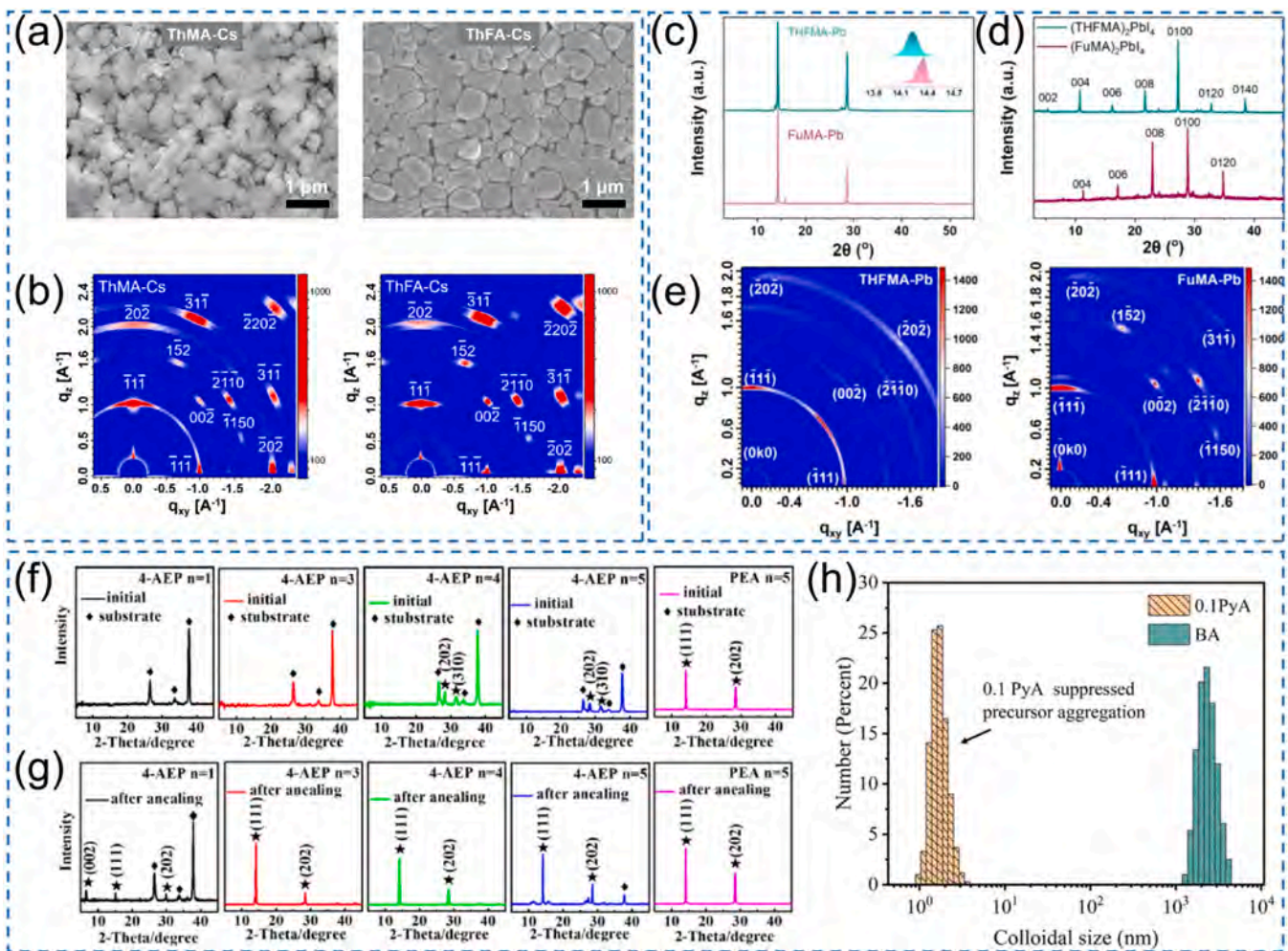
Fig. 5. (a) SEM image of ThMA-Cs and ThFA-Cs perovskite films. (b) GIWAXS results of ThMA-Cs and ThFA-Cs perovskite films. (c) XRD results of THFMA-based and FuMA-based 2D perovskite films. (d) XRD patterns of $(THFMA)_2PbI_4$ and $(FuMA)_2PbI_4$ crystal powders. (e) GIWAXS results of THFMA-based and FuMA-based 2D perovskite films. (f) XRD patterns of $(4-AEP)_2MA_{n-1}Pb_nI_{3n+1}$ ($n = 1, 3, 4, 5$) and $(PEA)_2MA_4Pb_5I_{16}$ perovskite films before thermal annealing and (g) after thermal annealing. (h) Laser particle size measurement results of the BA perovskite and 0.1PyA perovskite precursor solution. (a, b) Reproduced with permission from Ref. [70]. Copyright 2022, American Chemical Society. (c-e) Reproduced with permission from Ref. [74]. Copyright 2022, American Chemical Society. (f-h) Reproduced with permission from Ref. [66]. Copyright 2019, American Chemical Society.

indicated that ThFA-Cs and ThMA-Cs perovskite films exhibited high crystallinity with a preferred vertical orientation. Stability assessments performed over 720 h revealed that perovskite films based on ThMA and ThFA exhibited an unchanged phase, highlighting enhanced stability. This improved stability can be attributed to the incorporation of organic spacer cations, effectively alleviating inherent stress within the 3D $CsPbI_3$ perovskite structure. Ultimately, the PSC device utilizing ThFA-Cs-based perovskite films demonstrated an outstanding PCE of 16.00 %.

The furan ring, analogous to the thiophene ring, represents a five-membered heterocyclic compound with an oxygen atom, whereas thiophene contains a sulfur atom. Despite their structural similarities, the heteroatom oxygen in furan has a greater electronegativity and a smaller radius than the sulfur atom in thiophene. These characteristics make furan a promising candidate for spacer cations in 2D RP perovskites. In a groundbreaking development, Zheng and colleagues introduced a furan-based spacer cation, 2-furfurylammonium (FuMA)(12), for the first time in 2022 [102]. Under the facilitation of MACl additives, the crystal grains within the 2D RP perovskite $(FuMA)_2(MA)_4Pb_5I_{16}$ films exhibited an enhanced orientation of growth perpendicular to the substrate and larger size, which resulted in an improvement of PCE from 4.9 % to 15.66 % for PSCs. Notably, even when fabricating a 2D RP

perovskite device under ambient air conditions, the PCE can still achieve an impressive value of up to 15.24 %. Tetrahydrofuran (THF) is structurally similar to furan, with both compounds possessing five-membered rings containing an oxygen atom. However, the absence of aromaticity in THF distinguishes it from furan. In the same year, Liu and his co-workers developed a novel spacer cation, (tetrahydrofuran-2-yl) methanaminium chloride (THFMACl), and investigated its differences from FuMA in the context of perovskite films and device application [74]. The results showed that the observed shift of peaks in XRD tests of FuMA-based perovskite films towards higher 2θ angles, as shown in Fig. 5c, d compared with THFMA-based perovskite film, suggesting lattice compression. This compression can be attributed to the slight reduction in the size of the five-membered ring in FuMA, coupled with its enhanced intermolecular forces of $\pi - \pi$. The analysis through GIWAXS displayed sharp Bragg spots in FuMA-based perovskite films, suggesting their high crystallinity and vertical growth direction related to the substrate (Fig. 5e). The HRTEM and fast Fourier transform (FFT) measurements showed different phases ($n = 1, 2, 3, 4 \ldots$) coexisting in FuMA- and THFMA-based 2D perovskite films. Finally, the PCE of FuMA-based perovskite devices, utilizing an ITO/PEDOT: PSS/(Fu-MA)$_2$MA$_3$Pb$_4$I$_9$Cl$_4$/PCBM/BCP/Ag architecture, achieved a remarkable value of 18.00 %, which surpassed that of THF-based perovskite devices

and also exceeded the PCE reported by Zheng et al. for FuMA-based PSCs with an ITO/SnO₂/(FuMA)₂(MA)₄Pb₅I₁₆/Spiro-OMeTAD/Au structure.

Selenium, an element of the chalcogen family, along with sulfur and oxygen, possesses a larger atomic radius than its counterparts. This large size leads to a greater dipole moment in selenium-containing five-membered rings, specifically in selenophene. Notably, selenophene exhibits pronounced Se-Se interactions in various organic electronic materials [107,108]. Due to these properties, selenophene shows potential as a spacer cation in 2D RP perovskites. In 2023, Liu's group synthesized selenophene-based ammonium cation (SeMA)(13) through a complex route [72]. Computational analysis revealed that SeMA had a dipole moment of 9.21 D, surpassing that of thiophene-based spacer (ThMA) at 8.51 D and furan-based spacer (FuMA) at 7.73 D using the same calculation method. This higher dipole moment was believed to reduce the influence of quantum confinement between organic and inorganic layers. Using the normal spin-coating method, 2D RP perovskite films of $n = 5$ (SeMA)₂MA₄Pb₅I₁₅₋ₓClₓ were obtained. Comparing these perovskite films with MAPbI₃ perovskite films, XPS testing indicated a directional shift towards lower energy in the characteristic peak representing the binding energy of Pb. This shift suggested alterations in the chemical environment of Pb. PL and UV–vis absorption spectra revealed the presence of multiple phases ranging from low $n = 1$ phase to high n phases in SeMA-based perovskite films. Surface morphology analysis through SEM exhibited compact and smooth surfaces, while XRD and GIWAX analyses confirmed the vertical growth direction of crystal grains. This study's highlight was using predeposition transport layer (PDTL) techniques based on newly designed cations to mitigate surface defects in 2D RP SeMA-based perovskite films. This approach significantly enhanced the charge carrier mobility and reduced non-radiative recombination processes in the perovskite films. Consequently, the PCE of SeMA-based perovskite solar cells reached high values of 17.25 % and 19.03 %, using methylammonium (MA) and formamidinium (FA) as the A site cation in 2D RP perovskites, respectively.

Recent studies have explored using thiophene-, furan-, and selenophene-based spacer cations (ThMA, FuMA, and SeMA) as the organic layer in 2D RP perovskites. These spacer cations have shown a similar effect on the perovskite films' morphology and grain growth orientation. Specifically, they can promote the formation of large crystalline grains and induce a preferential vertical growth direction, thereby enhancing the performance of devices. However, despite these similarities, a detailed investigation into the subtle differences among these three spacer cations in the context of 2D RP perovskites is currently lacking, according to our knowledge. Moreover, we think exploring the interactions between different five-membered heterocycles based on S, O, and Se atoms in 2D RP perovskite may be a direction worthy of exploration.

In addition to aromatic rings incorporating heteroatoms derived from chalcogen elements, the potential of other heterocycles as spacer cations in 2D RP perovskites, such as the pyridine ring, remains largely unexplored. Compared with amino group, the nitrogen atom on the pyridine ring is more difficult to be protonated, which requires higher temperature for successful protonation. This limitation means that only the amino group can be protonated under conventional conditions for preparing spacer ammonium ions. A breakthrough was made by Wang et al. in 2019, who discovered a pyridine-based spacer cation known as 4-(aminoethyl)-pyridine (4-AEP)(15) [66]. They found that 4-AEP can modulate the crystallization rate of 2D RP perovskite films. To investigate the impact of 4-AEP on perovskite films, the authors prepared a series of films with the formula (4-AEP)₂MAₙ₋₁PbₙI₃ₙ₊₁ ($n = 1, 3, 4, 5$) and (PEA)₂MAₙ₋₁PbₙI₃ₙ₊₁ ($n = 5$). XRD analysis revealed that, before annealing, 2D RP perovskite films based on 4-AEP exhibited weak or negligible peaks, except for the substrate diffraction peak (Fig. 5f). However, after annealing, two distinct characteristic peaks, (111) and (202), emerged (Fig. 5g). In contrast, 2D perovskite films based on PEA displayed evident perovskite characteristic peaks of (111) and (202) even before annealing. These results suggested that compared to PEA

spacer cations, 4-AEP spacer cations could slow down the crystallization rate of perovskite films before annealing, which can facilitate the formation of high-quality perovskite films with dense and smooth surfaces, as confirmed by SEM measurements. Further analyses using FTIR and XPS techniques indicated that the nitrogen atoms within the pyridine ring can effectively coordinate with Pb ions in PbI₂, forming an intermediate species that decelerated the crystallization rate. The resulting PSCs based on (4-AEP)₂MAₙ₋₁PbₙI₃ₙ₊₁ ($n = 5$) exhibited a PCE of 11.68 % and improved moisture stability. Another pyridine-based spacer cation, 4-pyridinylmethylammonium (PyA)(14), with a shorter alkyl chain compared to 4-AEP, was introduced by Xu and his co-workers in 2022 [68]. They combined PyA spacer with the aliphatic spacer BA to prepare a mixed spacer 2D RP perovskite, namely (BA₁₋ₓPyAₓ)₂-MA₃Pb₄I₁₃ ($x = 0, 0.1, 0.2, 0.4$). The pure BA-based 2D RP perovskite served as a reference sample. Morphological characterization revealed obvious cracks in the BA-based 2D perovskite film. However, with the addition of PyA at a 0.1 ratio, uniformly smooth 2D perovskite films were obtained, and the cracks disappeared. As the PyA ratio increased from 0.1 to 0.4, the perovskite film quality deteriorated. Therefore, the optimal PyA ratio was determined to be 0.1. Laser particle size analysis demonstrated that the presence of the PyA spacer had an inhibitory effect on the formation of large colloidal particles in the precursor solution. This was evidenced by the larger colloidal size (> 1000 nm) observed in the BA-based 2D perovskite precursor solution compared to the 0.1PyA-based 2D perovskite precursor solution (5 nm) (Fig. 5h). Suppressed precursor aggregation contributed to the formation of large grains, reducing defects and nonradiative recombination. Consequently, the 0.1PyA-based solar cells achieved an impressive PCE of 13.01 % and exhibited high stability.

2.3. Substituents on aromatic rings

The substitution of specific functional groups (-F, -Br, -Cl, -OCH₃, -CF₃, etc.) for hydrogen on the benzene ring is an essential strategy for developing novel spacer cations, enhancing the performance, and improving the stability of 2D RP perovskites. Different substituents exhibit varying electron-withdrawing abilities, hydrophobicity, and size, leading to distinct effects on the properties of the substituted benzene ring. For instance, fluorine atoms can increase the dipole moment of benzyl spacer cations, thereby reducing the mismatch in dielectric constants between the organic and inorganic layers in 2D RP perovskites. Methoxy groups (-OCH₃) exhibit strong hydrophobicity, contributing to the stability of the 2D RP perovskite lattice. Furthermore, these substituents also impact the size of 2D RP perovskite crystal grains, growth orientation, exciton separation, charge carrier transport, etc.

Within the halogen group, fluorine (F) stands out due to its minimal atomic volume and strong electron-withdrawing ability. Consequently, extensive research has been conducted on fluorine-substituted spacer cations for use in 2D RP perovskites. The simplest fluorinated benzyl spacer cation is 4-fluorophenethylamine (4F-PEA)(16), which is believed to enhance the charge transfer ability between inorganic octahedral layers [62,67,80]. For example, Zhu et al. conducted an in-depth investigation into the structural and performance differences of 2D RP perovskite based on 4F-PEA and PEA to study the impact of fluorine atoms [80]. Initially, the author prepared 2D RP perovskite solar cells of $n = 1$ (4F-PEA)₂PbI₄ and (PEA)₂PbI₄ with identical structures based on PEA and 4F-PEA. The results showed that devices of (4F-PEA)₂PbI₄ exhibited a higher PCE of 1.90 %, compared with PCE of 1.34 % of (PEA)₂PbI₄. The measurement of time-resolved microwave conductivity (TRMC) also displayed about 7 times out-of-plane microwave mobility of (4F-PEA)₂PbI₄ than that of (PEA)₂PbI₄, which meant enhanced out-of-plane charge transfer capability for (4F-PEA)₂PbI₄ (Fig. 6a). Furthermore, from the perspective of single crystal structure analysis, as shown in Fig. 6b, in organic layers of (4F-PEA)₂PbI₄, the 4-FPEA cations adopted a face-to-face stacking arrangement. In contrast,
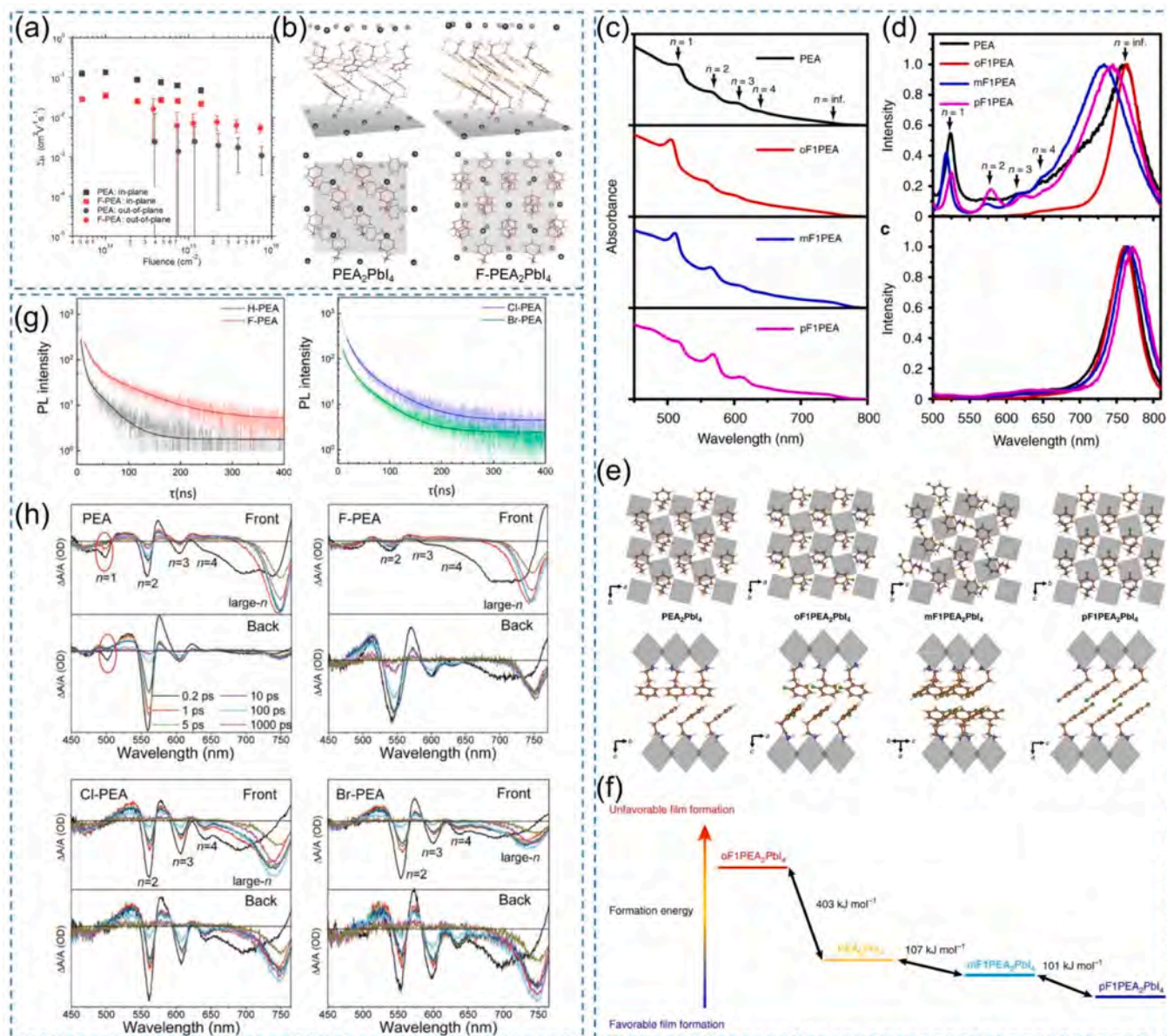
Fig. 6. (a) TRMC comparison of out-of-plane and in-plane transport for $(PEA)_2PbI_4$ and $(4F\text{-}PEA)_2PbI_4$ films. (b) Single crystal structures of $(PEA)_2PbI_4$ and $(4F\text{-}PEA)_2PbI_4$. (c) UV–vis absorption and (d) PL peak from the back side (top) and the front side (bottom) of PEA-, oF1PEA-, mF1PEA-, and pF1PEA-based 2D perovskites ($n = 4$). (e) Single crystal structures of $(PEA)_2PbI_4$, $(oF1PEA)_2PbI_4$, $(mF1PEA)_2PbI_4$ and $(pF1PEA)_2PbI_4$. (f) Calculated formation energy for $(PEA)_2PbI_4$, $(oF1PEA)_2PbI_4$, $(mF1PEA)_2PbI_4$ and $(pF1PEA)_2PbI_4$. (g) PL decay profiles of PEA-, 4F-PEA-, 4Cl-PEA-, and 4Br-PEA-based 2D RP perovskites on the glass substrate. (h) TA spectra at different delay times with top and bottom excitation for PEA-, 4F-PEA-, 4Cl-PEA-, and 4Br-PEA-based 2D RP perovskites films. (a, b) Reproduced with permission from Ref. [80]. Copyright 2019, American Chemical Society. (c-f) Reproduced with permission from Ref. [109]. Copyright 2022, Springer Nature. (g) Reproduced with permission from Ref. [46]. Copyright 2019, American Chemical Society. (h) Reproduced with permission from Ref. [81]. Copyright 2020, Wiley-VCH.

the stacking arrangement was edge-to-face for $(PEA)_2PbI_4$. By comparison with edge-to-face packing, face-to-face packing could lead to reducing the ring centroid-to-centroid distances for 4F-PEA spacers and increased pi-orbital overlap, which was conducive to the charge transport in the out-of-plane direction. Additionally, a comparative analysis was also undertaken for high n-value ($n = 5$) perovskites based on 4F-PEA and PEA, $(4F\text{-}PEA)_2MA_4Pb_5I_{16}$ and $(PEA)_2MA_4Pb_5I_{16}$. Surface morphology tests indicated that $(4F\text{-}PEA)_2MA_4Pb_5I_{16}$ films had a more homogeneous surface with reduced grain boundaries compared to $(PEA)_2MA_4Pb_5I_{16}$ films. Results from TPRL and TRMC tests demonstrated that $(4F\text{-}PEA)_2MA_4Pb_5I_{16}$ possessed extended carrier lifetimes and reduced defect density. The improvements in stacking, morphology, and electronic performance were attributed to the introduction of

fluorine atoms, which ultimately resulted in an improved PCE of 13.64 % for solar cells based on $(4F\text{-}PEA)_2MA_4Pb_5I_{16}$. But the $(PEA)_2MA_4Pb_5I_{16}$-based PSCs only had a PCE of 9.6 %. More importantly, due to the hydrophobicity induced by fluorination, the $(4F\text{-}PEA)_2MA_4Pb_5I_{16}$-based devices showed higher stability than $(PEA)_2MA_4Pb_5I_{16}$-based devices under high temperature and ambient conditions. In another study by Shao et al., with the assistance of NH_4SCN additives, the PCE of solar cells based on $(4F\text{-}PEA)_2MA_4Pb_5I_{16}$ further achieved a breakthrough [62], reaching 17.3 %. It is worth mentioning that Shao's work additionally pointed out that fluorinated spacer cations 4F-PEA can induce systematically distributed patterns for different n-phases in 2D RP perovskites films. Specifically, the low n-phases were observed at the bottom, while the high n-phases were

located at the top surface, which proved advantageous for charge separation and transport. In Liu's research, a fluorine atom was introduced at the para-position of FA-based spacer (Benzamidine (PhFA)), resulting in a new aromatic spacer, 4-Fluoro-benzamidine (p-FPhFA)(24) [67]. Similarly, introducing fluorine at the para-position significantly enhanced the quality of the 2D perovskite thin film and promoted grain growth perpendicular to the substrate. Non-radiative recombination was suppressed, whereas the mobility and lifetime of the carriers were improved. Ultimately, PSCs with p-FPhFA spacers pushed the PCE to 17.37 %.

The position of fluorine substitution on the benzene ring is critical to the 2D perovskite structure and morphology, as well as the performance of the corresponding prepared solar cells [71,109,110]. You and co-workers had conducted in-depth research on 2D RP perovskites based on monofluorinated PEA with different substitution positions of benzene moiety (2-fluorophenethylammonium (oF1PEA)(18), 3-fluorophenethylammonium (mF1PEA)(17) and 4-fluorophenethylammonium (pF1PEA/4F-PEA)) [109]. UV testing revealed distinct distributions of different n phases within oF1PEA, mF1PEA, and pF1PEA 2D perovskite films (Fig. 6c). Also, PL characterization, excited from both front and back sides, indicated that high-n phases perovskites were concentrated near the surface in contact with air, while low-n phases perovskites were located at the bottom for 2D perovskite films with mF1PEA and pF1PEA spacers, as shown in (Fig. 6d). However, in oF1PEA-based 2D perovskite films, the distribution of n phases was random. Compared to the uniform surface of PEA-based 2D perovskite films with few pinholes, oF1PEA-based 2D perovskite films had a rough and uneven surface. Nonetheless, mF1PEA and pF1PEA-based 2D perovskite films were uniform and smooth. Furthermore, 2D perovskite single crystals (Fig. 6e) with $n = 1$ for PEA, oF1PEA, mF1PEA, and pF1PEA were synthesized to study their differences in molecular stacking and the interlayer interactions between inorganic octahedral layers and organic layers. It is noted that in pF1PEA$_2$PbI$_4$, these spacer cations between adjacent organic layers exhibited a completely ordered face-to-face stacking arrangement. However, in the single layer of mF1PEA cations in mF1PEA$_2$PbI$_4$, there was a rotation in the angle between adjacent aromatic cation groups, which led to a form of herringbone arrangement. The oF1PEA$_2$PbI$_4$ and PEA$_2$PbI$_4$ had a similar structure, where the spacer cations between adjacent organic layers were arranged in an edge-to-face stacking manner. The calculated formation energy ((Fig. 6f)) based on these single crystals showed a trend related to crystal stacking and disorder: pF1PEA$_2$PbI$_4$ > mF1PEA$_2$PbI$_4$ > PEA$_2$PbI$_4$ > oF1PEA$_2$PbI$_4$. These differences were possibly caused by different dipole-dipole interactions, resulting in the variations of PCE of solar cells based on these spacer cations. As a result, pF1PEA- and oF1PEA-based PSCs showed the highest and lowest PCEs, at over 10 % and below 1 %, respectively. Another parallel research (22, 23, 24) focusing on the disparate effects of fluorine substitution at various positions of benyl moiety in 2D RP perovskites was predicated on PMA cations and was conducted by Zhang et al. [71]. In this research endeavor, the influence of fluorine substitution at distinct positions on the morphology, phase distribution, crystallinity, and device performance of 2D RP perovskite films closely aligned with the findings in You's work. Similarly, solar cells fabricated based on fluorine substitution at the para position of the benzene ring in PMA demonstrated the highest PCE of 17.12 %.

Aside from fluorine, which belongs to the halogen family, chlorine and bromine have different atomic radius and electronegativities. In the study conducted by Huang et al., they used 3-bromobenzylammonium iodide (3BBAI)(25) to prepare 2D RP perovskites and achieved high PCE of 18.2 % for corresponding solar cells [75]. They indicated that 3BBA can result in the distribution of low n phases at the bottom of film and high n phases at the top of film, which is benefited to the charge transportation. Subsequently, Wang et al. investigated the impact of chloro (Cl), and bromo (Br) substitutions on the para position in PEA cations in 2D RP perovskites [46]. They designed a series of spacer cations, namely PEA, 4F-PEA, 4Cl-PEA (20), and 4Br-PEA (21), and

calculated dipole moments for them were approximately 11.83 D, 13.16 D, 13.49 D, and 13.34 D, respectively. It could be seen that the introduction of halogen atoms with electron-withdrawing properties increased the dipole moment, which can benefit charge dissociation and intramolecular charge transport. Subsequently, they prepared corresponding 2D RP perovskite films with a fixed n value of 3 using these spacer cations, PEA$_2$MA$_2$Pb$_3$I$_{10}$, 4F-PEA$_2$MA$_2$Pb$_3$I$_{10}$, 4Cl-PEA$_2$MA$_2$Pb$_3$I$_{10}$, and 4Br-PEA$_2$MA$_2$Pb$_3$I$_{10}$. XRD and GIWAX measurements revealed that H-PEA$_2$MA$_2$Pb$_3$I$_{10}$ and 4F-PEA$_2$MA$_2$Pb$_3$I$_{10}$ films possessed a preferential growth orientation perpendicular to the substrate compared to 4Cl-PEA$_2$MA$_2$Pb$_3$I$_{10}$ and 4Br-PEA$_2$MA$_2$Pb$_3$I$_{10}$ films. This difference may be because the radius of the Cl and Br atoms is larger than that of the H atom and F atom. The structural analysis for PEA$_2$PbI$_4$, 4F-PEA$_2$PbI$_4$, 4Cl-PEA$_2$PbI$_4$, and 4Br-PEA$_2$PbI$_4$ single crystals was conducted to study the distortion in the perovskite inorganic octahedral structure. The results indicated that the angle of Pb–I–Pb changed from 151.3 ° for PEA$_2$PbI$_4$ to 152.91 ° for 4F-PEA$_2$PbI$_4$, then to 153.6 ° for 4Cl-PEA$_2$PbI$_4$ and finally to 152.6 ° for 4Br-PEA$_2$PbI$_4$. The smaller Pb–I–Pb angle indicated a stronger influence of spacer cations on the PbI$_6$ octahedra. And the exciton-binding energy, characterized by PL lifetime test, showed a clear difference in the order of PEA$_2$PbI$_4$ > 4Br-PEA$_2$PbI$_4$ > 4Cl-PEA$_2$PbI$_4$ > 4F-PEA$_2$PbI$_4$, as shown in Fig. 6g. Among these perovskites, the solar cells based on 4F-PEA$_2$MA$_2$Pb$_3$I$_{10}$ films obtained the highest PCE of 5.83 %. This study pointed out that the appropriate selection for electron-withdrawing atomic substituents can be used to regulate the optoelectronic performance of the devices. Zheng et al. conducted further research on utilizing these four spacer cations in 2D RP perovskites with fixed $n = 4$ [81]. Their research underscored the ordered gradient arrangement of different n-values within PEA- and 4F-PEA-based perovskite thin films due to nucleation competition between high n phases and low n phases. From the bottom to the top of the perovskite film, there was a gradual increase in the n value of the perovskite phases, leading to the formation of graded band arrangement, which ultimately facilitated more efficient charge transportation (Fig. 6h). However, for 4Cl-PEA- and 4Br-PEA-based perovskite thin films, the distribution of high n phases and low n phases was random, generating a disorderly band arrangement. Similar to Wang's work, in Zheng's findings, 4F-PEA-based perovskite solar cells achieved the highest PCE at 18.10 %, followed by a PCE of 12.23 % for PEA-based solar cells. Solar cells based on 4Cl-PEA and 4Br-PEA showed the worst performance, with PCEs recorded at 7.93 % and 6.08 %, respectively. In addition, the results of stability measurements showed that devices employing these four spacer cations exhibited commendable moisture stability versus 3D perovskites. However, in terms of thermal stability, solar cells based on PEA and 4F-PEA notably outperformed those based on 4Cl-PEA and 4Br-PEA, possibly due to the disorderly distribution of different n-phases.

In addition to investigating substituents from the halogen group, which possess high electron-withdrawing characteristics, substituents with electron-donating abilities, such as methoxy groups, have also been explored. For example, Fu et al. chose F and MeO (19) as substituents for the para-position hydrogen atoms on benzene ring of PEA and constructed three different 2D RP perovskites with $n = 5$, (4F-PEA)$_2$(MA)$_4$Pb$_5$I$_{16}$, (PEA)$_2$(MA)$_4$Pb$_5$I$_{16}$ and (MeO-PEA)$_2$(MA)$_4$Pb$_5$I$_{16}$ [111]. Regarding stability, 2D perovskite films utilizing 4F-PEA and MeO-PEA as spacer cations demonstrated superior performance compared to PEA-based perovskite films (Fig. 7a-b). The authors conducted computational calculations to determine the specific reasons for this observation. The results suggested that the enhanced stability of the MeO-PEA-based 2D perovskite could be attributed to the significant volume of the MeO group, which imparts a certain repulsive effect on water molecules. On the other hand, despite the small size of the F atom as the substituent in 4F-PEA cations, its electronegativity can still induce a repulsive effect on water molecules, thereby contributing to the improved stability of the 4F-PEA-based perovskite. However, while MeO increased the resistance of the perovskite lattice to water, it
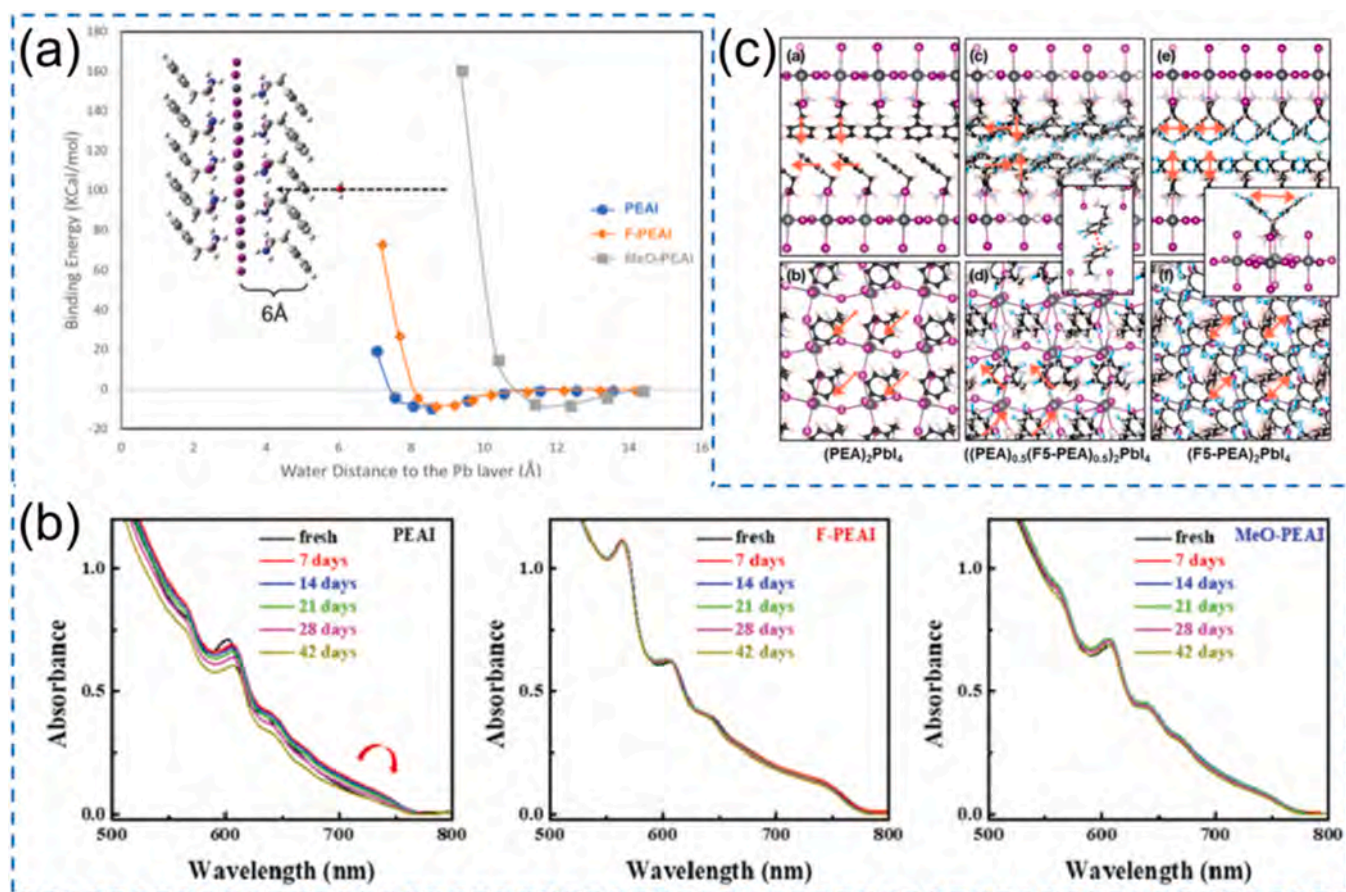
Fig. 7. (a) The binding energy curves of water and perovskites with PEA, 4F-PEA, and MeO-PEA spacer ligands. (b) Absorption spectra of PEA-, 4F-PEA-, and MeO-PEA-based 2D RP perovskites under humidity conditions of 40 – 50 %. (c) Single-crystal structures of $(PEA)_2PbI_4$, $((PEA)_{0.5}(F5-PEA)_{0.5})_2PbI_4$ and $(F5-PEA)_2PbI_4$. (a, b) Reproduced with permission from Ref. [111]. Copyright 2019, Wiley-VCH (c) Reproduced with permission from Ref. [112]. Copyright 2019, American Chemical Society.

simultaneously negatively impacted the performance of the perovskite devices due to its large volume. This effect resulted in a low PCE of 9.4 % for MeO-PEA-based solar cells. Among the devices based on these three spacer cations, solar cells utilizing 4F-PEA as spacers achieved the highest PCE at 13.5 %.

Another spacer cation developed for 2D RP perovskites is 2,3,4,5,6-pentafluorophenethylammonium (F5-PEA)(27), which is a derivative of PEA where all hydrogen atoms on the phenyl ring are replaced by fluorine [112,113]. In a study by You et al., mixed cation 2D RP perovskites with $n = 4$ were prepared using PEA and F5-PEA cations [112]. After adjusting the ratio of the two spacer cations, the authors found that the optimal performance of the 2D perovskite thin films was optimal when the ratio of PEA to F5-PEA was 1:1. Deviation from this ratio, either above (1: 0.75) or below (0.75: 1), resulted in a decrease in device performance. Under the 1:1 ratio of PEA to F5-PEA, the surface of the 2D perovskite thin films was made uniform and smooth without any holes, and it exhibited an ordered vertical distribution of different phases. At the optimal ratio, 2D perovskite solar cells displayed a high PCE exceeding 10 % with enhanced stability. Further single-crystal testing results for $(PEA)_2PbI_4$, $((PEA)_{0.5}(F5-PEA)_{0.5})_2PbI_4$, and $(F5-PEA)_2PbI_4$ revealed that only a face-to-face stacking structure was observed in $((PEA)_{0.5}(F5-PEA)_{0.5})_2PbI_4$ as shown in Fig. 7c. This result was caused by quadrupole−quadrupole interactions between PEA and F5-PEA, leading to the stabilization of the perovskite lattice and enhancement of device performance.

2.4. Multiple aromatic rings

The successful application of single-ring aromatic spacer cations in 2D RP perovskites has sparked interest in investigating multiple-ring aromatic spacer cations [73,77,79,114,115]. By leveraging the high dipole moment resulting from extended π-electron delocalization, incorporating multiple aromatic ring amines offers the potential to mitigate the dielectric mismatch between organic and inorganic layers, thereby minimizing the effects of quantum confinement. However, the research on multiple-ring aromatic organic amines is relatively scarce, primarily focusing on naphthyl-based and bithiophene-based ammonium ions, which have already demonstrated significant practical applications. As such, exploring the applicability of other multi-ring aromatic amines in this context is still necessary.

Xu and his colleagues used 1-naphthalenemethylammonium (NpMA) (28) and 9-anthracenemethylammonium (AnMA)(29) as spacer cations to fabricate 2D RP perovskite thin films and corresponding devices with a normal n value of 4 [73]. They confirmed the existence of $N - H \cdots I$ interactions between the spacer ammonium ion and the inorganic octahedra framework through ^1H NMR measurements (Fig. 8a). The PL and UV−vis absorption spectrum indicated that different n phases coexisted in NpMA-based 2D perovskite films, further verified by HRTEM tests as shown in Fig. 8b. But in the AnMA-based 2D perovskite films, 3D-like phases were dominated, possibly owing to bulk steric effects of AnMA spacer. Besides, the perovskite films based on NpMA exhibited superior crystallinity and vertical growth orientation to the substrate. Utilizing TA spectroscopy, the authors clarified the charge transport pathways within 2D perovskites. They proposed that
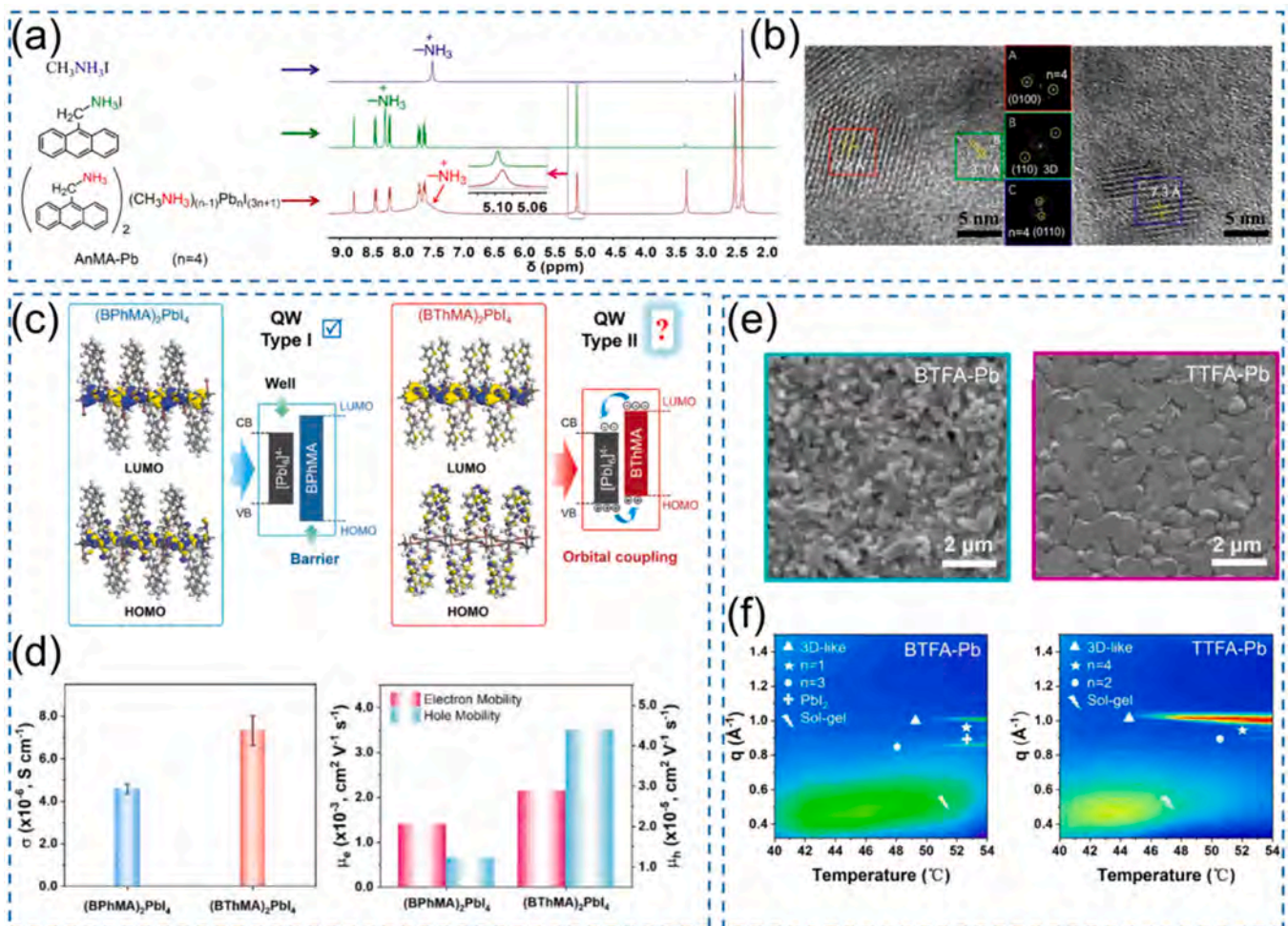
Fig. 8. (a) Chemical structure and corresponding ^{1}H NMR spectra of MAI, AnMAI, and $(AnMA)_2MA_3Pb_4I_{13}$. (b) HRTEM image of the NpMA-based (left) and AnMA-based 2D perovskite films (right). (c) Calculated HOMO and LUMO results for $(BPhMA)_2PbI_4$ and $(BThMA)_2PbI_4$ and proposed energy levels of organic and inorganic components, and conductivity and statistics of mobilities diagrams (d) of corresponding 2D RP perovskite films. (e) SEM images of the BTFA-based and TTFA-based 2D RP perovskite films. (f) The structural evolution monitored by in situ GIWAXS during the heating from 40 °C to 54 °C at a rate of 1 °C/30 s of the as-deposited BTFA-based and TTFA-based 2D perovskite films. (a, b) Reproduced with permission from Ref. [73]. Copyright 2020, American Chemical Society. (c, d) Reproduced with permission from Ref. [77]. Copyright 2023, Wiley-VCH. (e, f) Reproduced with permission from Ref. [79]. Copyright 2023, Wiley-VCH.

photoexcited excitons originating from the low-n phases initially migrated to the neighboring high-n phases, subsequently dissociating into free charges. The 2D PSCs with NpMA and AnMA achieved a PCE of 17.25 % and 14.47 % with long-term stability, respectively. Similar to NpMA, 1-naphthylamine (1-NA)(30) was also developed into spacer cation to prepare Cs-based solar cells with $n = 4$ by Jin et al., achieving an impressive PCE of 16.62 %. The authors pointed out that compared with the common PEA cations, 1-NA can further reduce the binding energy of 2D perovskites, thereby promoting the dissociation of excitons. In addition, they also suggested that the strong π-π interactions not only enhanced the stability of perovskite lattices but also facilitated the formation of high-quality films with vertical orientation, which improved device performance.

Yuan et al. designed a novel spacer derived from carbazole, (9H-carbazol-9-yl)butyl-1-ammonium (CA)(35), and used it into 2D RP perovskites with $n = 5$ [75]. Employing the anti-solvent method, they induced a distribution of low n phases at the top of perovskite film, which led to outstanding stability against water. Besides, under the assistance of NH$_4$SCN additives, the perovskite crystals can grow in the vertical orientation, resulting in the enhanced carrier transport ability and reduced non-radiative recombination. Finally, the PSCs based on CA had an excellent PCE of 18.23 % and long-term stability.

Recently, Liu et al. utilized bithiophenemethylammonium(BThMA)

(33) and biphenemethylammonium (BPhMA)(34) in 2D RP perovskites as spacer cations, and they arrived at a concept of "quantum confinement breaking" [77]. To be specific, through the DFT calculation results, as shown in Fig. 8c-d based on perovskite structure of $n = 1$, they discovered that there was a strong orbital coupling for (BThMA)PbI$_4$ between the octahedral framework of inorganic layers and organic conjugated molecular layers, derived from the fact that its HOMO was located in inorganic layers. In contrast, LUMO was mainly located in molecule layers. However, no such coupling was seen in (BPhMA)$_2$PbI$_4$ perovskites because both its HOMO and LUMO were located in the inorganic octahedra layers. Owing to this orbital coupling, (BThMA)PbI$_4$ showed enhanced conductivity and electron and hole mobility compared with (BPhMA)$_2$PbI$_4$ in the direction vertical to the substrate. In the study for perovskites with higher n values, BThMA-based 2D perovskite films displayed superior crystallinity and uniform surfaces with large grains. As a result, the PCE of PSCs based on the BThMA spacer had an impressive value of 18.05 %, higher than that of BPhMA-based devices (12.69 %). This work provided a novel thought to address or impair the quantum confinement effect in 2D RP perovskites. In another research conducted by Liu et al., they combined fused-bithiophene and unfused-bithiophene with the FA group to develop FA-based multiple aromatic ring spacer cations, TTFA(31) and BTFA(32) [79]. This research focused on studying the nucleation and

crystallization process for 2D perovskite films through situ GIWAXS and optical microscopy measurement (Fig. 8e-f). The authors discovered that the binding energy E_b of TTFA between contiguous molecules was greater than that in BTFA, which led to larger clusters in 2D perovskite precursor solution based on TTFA. The larger clusters subsequently accelerated the formation of large crystal grains, generating high-quality films for TTFA-based 2D perovskite. In contrast, BTFA-based 2D perovskite films showed rough surface morphology accompanied by small grains. Differences in morphology ultimately resulted in variations in performance, with TTFA-based solar cells exhibiting a superior PCE of 19.41 %.

3. Aromatic diamine spacer cations of 2D DJ perovskites

Recently, there has been a marked increase in the exploration of 2D DJ perovskites. The DJ-phase structure incorporates a divalent organic cation connecting each perovskite sheet layer, which results in a well-ordered lamellar structure. This phase contrasts with the RP phase perovskite structure, which displaces adjacent 2D perovskite sheet layers with half an octahedron. The DJ-phase structure enhances the structural stability of the 2D layered perovskite by completely occupying the van der Waals gaps in the RP lamellar structure, positioning it as a hopeful candidate for high-efficiency, stable perovskite devices. However, there have been relatively few research studies on aromatic

DJ-type diamine ions, which are primarily based on benzene and thiophene compounds. Therefore, although the development of DJ-type spacers can also be divided into four directions (similar to RP-type spacers), this section will discuss these spacers and corresponding perovskites from three aspects, benzene, thiophene, and pyridine derivatives.

3.1. Benzene derivatives

The divalent organic cation 1,4-phenylenedimethanam-monium (PDMA)(36) has been widely used to create 2D DJ-phase perovskites. The initial use of PDMA was realized by Gratzel et al. in 2019. They conducted a detailed study on the morphology and optoelectronic properties of 2D DJ (PDMA)FA$_{n-1}$Pb$_n$I$_{3n+1}$ perovskite films with different n values ($n = 1, 2, 3,$ and 4) [61]. As shown in Fig. 9a-b, with the value of n increases, the morphology of the 2D DJ perovskite films transitioned from large-sized grains ($n = 1$) to needle-like structures ($n = 2$) and finally to a similar island-like pattern covering the film surface ($n = 3$), indicating a weakening in the crystallinity of films. Decreased crystallinity was also corroborated by XRD testing. Besides, UV and PL exhibited a redshift phenomenon similar to RP-type perovskites as the value of n increases (Fig. 9c-d). A PCE exceeding 7 % was achieved in 2D DJ perovskite devices with n phase of 3, which also had extremely high air stability. Followingly, Etgar et al. Used PDMA spacers to prepare 2D
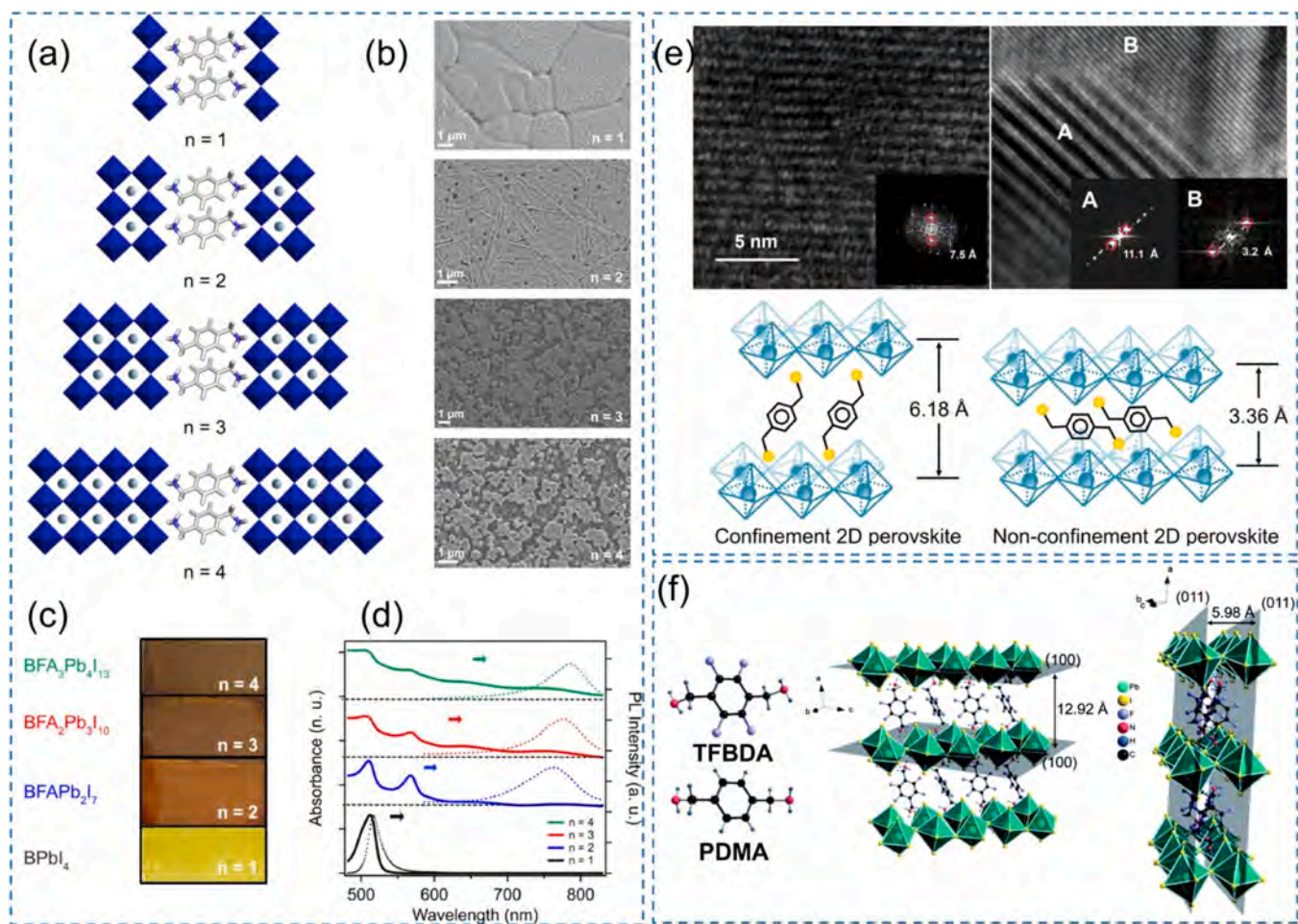

Fig. 9. (a) Schematic structure of (PDMA)FA$_{n-1}$Pb$_n$I$_{3n+1}$ perovskites with different n compositions ($n = 1 - 4$). (b) SEM images of (PDMA)FA$_{n-1}$Pb$_n$I$_{3n+1}$ perovskite films with different n compositions ($n = 1 - 4$). (c) Optical images of (PDMA)FA$_{n-1}$Pb$_n$I$_{3n+1}$ perovskite films with different n compositions ($n = 1 - 4$) and (d) the corresponding UV−vis absorption and PL spectra. (e) HR-TEM images and schematic crystal structures of the confinement 2D and non-confinement 2D perovskites. (f) Chemical structures of PDMA and TFBDA and single crystal structure of (TFBDA)PbI$_4$. (a-d) Reproduced with permission from Ref. [61]. Copyright 2019, American Chemical Society. (e) Reproduced with permission from Ref. [84]. Copyright 2019, Wiley-VCH. (f) Reproduced with permission from Ref. [87]. Copyright 2021, Wiley-VCH.

DJ perovskite devices with $n = 10$ and achieved an impressive PCE of 15.6 % without other molecules or additives [116]. They suggested that PDMA spacers played a crucial role in determining the orientation of the perovskite structure. In 2019, Liang's group investigated the inner lattice structures of PDMA-based 2D DJ perovskite [84]. They systematically explored the impact of varying the molar proportion of PDMA on the charge transport and crystal structure of perovskite films. The researchers found that when n <= 2, the structure of the 2D perovskite was either a confinement or nonconfinement mixture. However, when n > 2, the structure became entirely nonconfinement. This transformation was confirmed by HR-TEM measurements, as shown in Fig. 9e, and the reason can be attributed to the octahedral layers' extrusion of the PDMA spacer layer. Besides, the authors then compared the UV–vis absorption spectra for samples with n value ranging from 1 to 10. For samples of $n = 1$, 2, and 3, there were obvious exciton absorption peaks, but with n value increasing to higher, these peaks disappeared and a distinct absorption band edge emerged at higher wavelength, which was further evidence of the reduced quantum confinement effect. As illustrated in Fig. 9e, the spacing of inorganic layers in the nonconfinement structure was significantly shorter than that in the confinement structure. That was consistent with the calculated exciton binding energy of the nonconfinement structure (70 meV), less than that of the confinement structure (140 meV). Finally, the solar cells with an n value of 6 achieved the best PCE of 11 %. Moreover, Liu and co-workers also prepared 2D DJ perovskites using PDMA as spacers with an n value of 4. Their research highlighted the hot spin-coating method, which resulted in more uniform, high-quality thin films with a more orderly distribution of different n phases [85]. Carrier transport ability was increased, and a high PCE of 15.81 % was obtained for the corresponding devices.

As a fluorinated derivative of PDMA, 2,3,5,6-tetrafluoro-1,4-benzenedimethanammonium (TFBDA)(37) was designed, synthesized, and used to construct 2D DJ perovskites by Zheng et al. in 2021 [87]. As shown in Fig. 9f, the researchers found that the prepared (TFBDA)PbI$_4$ single crystal showed a layered structure, and the stack arrangement of the adjacent TFBDA^{2+} ligands was in an edge-to-face stacking way. Additionally, the TFBDA-based 2D DJ perovskite films preferentially grew in a vertical orientation, which caused a higher PCE of 15.24 % for PSCs with $n = 10$, larger than the PCE of BDA-based devices. Importantly, owing to the hydrophobic nature of the fluorinated cations, perovskite devices with spacers of TFBDA displayed increased long-term stability. Similarly, Liu's group also used TFBDA as a spacer cation to prepare 2D DJ perovskites devices with $n = 4$, achieving a higher PCE of 16.62 % [88]. Importantly, Liu and colleagues specifically pointed out from another point of view that the improved stability of perovskite devices based on TFBDA was due to the existence of multiple non-covalent interactions between TFBDA cations and octahedral layers, such as F…I, CH…F and NH…F interactions. This interaction greatly stabilized the lattice structure of 2D DJ perovskites.

In addition, 1,5-diaminonaphthalene (NDA)(38) with extended π-conjugation length was developed as spacer for 2D DJ perovskites by Satapathi et al. [86]. Under the assistance of NH$_4$SCN additives, NDA-based perovskite films had a better surface morphology and high crystallinity, which contributed to its decreased trap density and improved carrier transport ability. Notably, the solar cells based on NDA spacer reached an impressive value of 15.08 % and showed long-term stability against humidity and heat.

3.2. Aromatic heterocyclic derivatives

As previously discussed, thiophene is one of the most commonly used functional heterocycles, and its significant application value in 2D RP-type perovskites has already been demonstrated. Similarly, thiophene can also be applied in 2D DJ-type perovskites. In 2020, Liu et al. synthesized 2,5-thiophenedimethylammonium (ThDMA)(39) and constructed the 2D DJ perovskites with $n = 5$ [89]. They found that introducing a strong coordination molecule DMSO into the precursor

solution can effectively regulate the growth and orientation of 2D DJ perovskite crystals and improve the film morphology. The effect reduced the density of defective states and enhanced the carrier transport efficiency. The optimized devices achieved a notable PCE of 15.75 %. Subsequently, Liu et al. further developed a bithiophene-based spacer, namely thieno[3,2-b] thiophene-2,5-diyldimethanaminium (TTDMA) (40), and it was successfully used as a spacer cation for 2D DJ perovskites (Fig. 10a-b) [91]. The longer π-conjugation length of TTDMA compared to ThDMA resulted in enhanced intermolecular interactions between organic spacers in the layered 2D chalcogenide phases. Precursor aggregates of ~1 μm were detected in the TTDMA-Pb chalcogenide precursor solution, which led to the formation of large grain sizes in the perovskite thin films with enhanced crystallinity and vertical orientation as shown in Fig. 10c-d. In addition, the extended conjugate π length also led to a decrease in exciton binding energy, which was beneficial for efficient charge transfer. As shown in Fig. 10e, the ThDMA film displayed dominant n = 2 and n = 3 phases, while TTDMA film had dominant phases of n = 3 and n = 4. The ultrafast decay times of TTDMA films were $\tau_{1, n = 3} = 0.26$ ps and $\tau_{1, n = 4} = 13.18$ ps. Whereas, ThDMA film showed longer decay times of $\tau_{1,n = 2} = 0.32$ ps, $\tau_{1,n = 3} = 0.46$ ps, and $\tau_{1,n = 4} = 18.57$ ps. Ultimately, the PCE of TTDMA-based solar cells reached a high value of 18.82 %. In 2022, another new spacer cation with two covalently attached thiophene rings, namely bithiophene dimethylammonium (BThDMA)(41) was also successfully developed by Liu et al.. They investigated the interactions between the intermediate spacer and the inorganic layer [90]. The results showed that there were strong orbital interaction effects between the BThDMA spacer layers and the adjacent inorganic layers. This interaction could also induce the growth of crystals with large grains and preferential vertical orientation, which reduced the trap density and improved the charge carrier mobility. As a result, the perovskite devices based on BThDMA had an excellent PCE of 18.1 %.

Seferos et al. established structure-property relationships by tuning the structure of the rings (benzene and thiophene rings) and substituents of 2D DJ perovskite spacer molecules [117]. They firstly designed a symmetric conjugated linker structure [1,1′-biphenyl]−4,4′-diyl-dimethylamine (PP), and then the symmetry was disrupted by substituting in a sequence of fluorine atoms to achieve a structure of (2-fluoro-[1, 1′-biphenyl]−4,4′-diyl)-dimethylamine (FPP). In the end, heterocyclic substitution was employed to obtain a structure of (5-(4-(aminomethyl)−2-fluorophenyl)thiophene-2-yl)methanamine (FPT) (Fig. 10f). The large in-plane deformation of the octahedron was determined by the strength of the electrostatic interactions between the positively charged ends of the organic ligand and the negatively charged inorganic layer. This deformation resulted in a larger band gap which was represented by blue-shifted absorption and emission peaks. The authors verified that enhanced π-stacking interactions between conjugated organic ligands positively improved the stability of the structure.

As previously mentioned, the hydrogen on the pyridine ring can be protonated under high-temperature reaction conditions. In 2018, Kanatzidis et al. reported two novel diamine cations, 4-(aminomethyl) pyridinium (4AMPY)(42) and 3-(aminomethyl)pyridinium (4AMPY) (43), and applied them in 2D DJ perovskites [83]. The authors discovered that the varying positions of nitrogen in pyridine relative to the alkyl chain significantly impacted the crystal structure, as shown in Fig. 10g-j. Compared to 3AMPY, 4AMPY had higher symmetry, which can help maintain the octahedra's orderly arrangement in the inorganic layers (eclipsed conformation). Also, the adjacent 4APMY cations adopted a face-to-edge stacking in organic layers. As for 3AMPY, its asymmetry led to a slight misalignment of the inorganic layer. In contrast to 3AMPY, 4AMPY-based 2D DJ perovskite structure showed a smaller Pb-I-Pb angle and a larger distortion for the octahedral layers. Besides, the penetration depth of the NH$_3^+$ of 3AMPY into the inorganic layer was deeper than that of 4AMPY, which reduced the spacing between inorganic layers and led to a small band gap. It is worth noting that as the value of n increased, the Pb-I-Pb angle increased for both
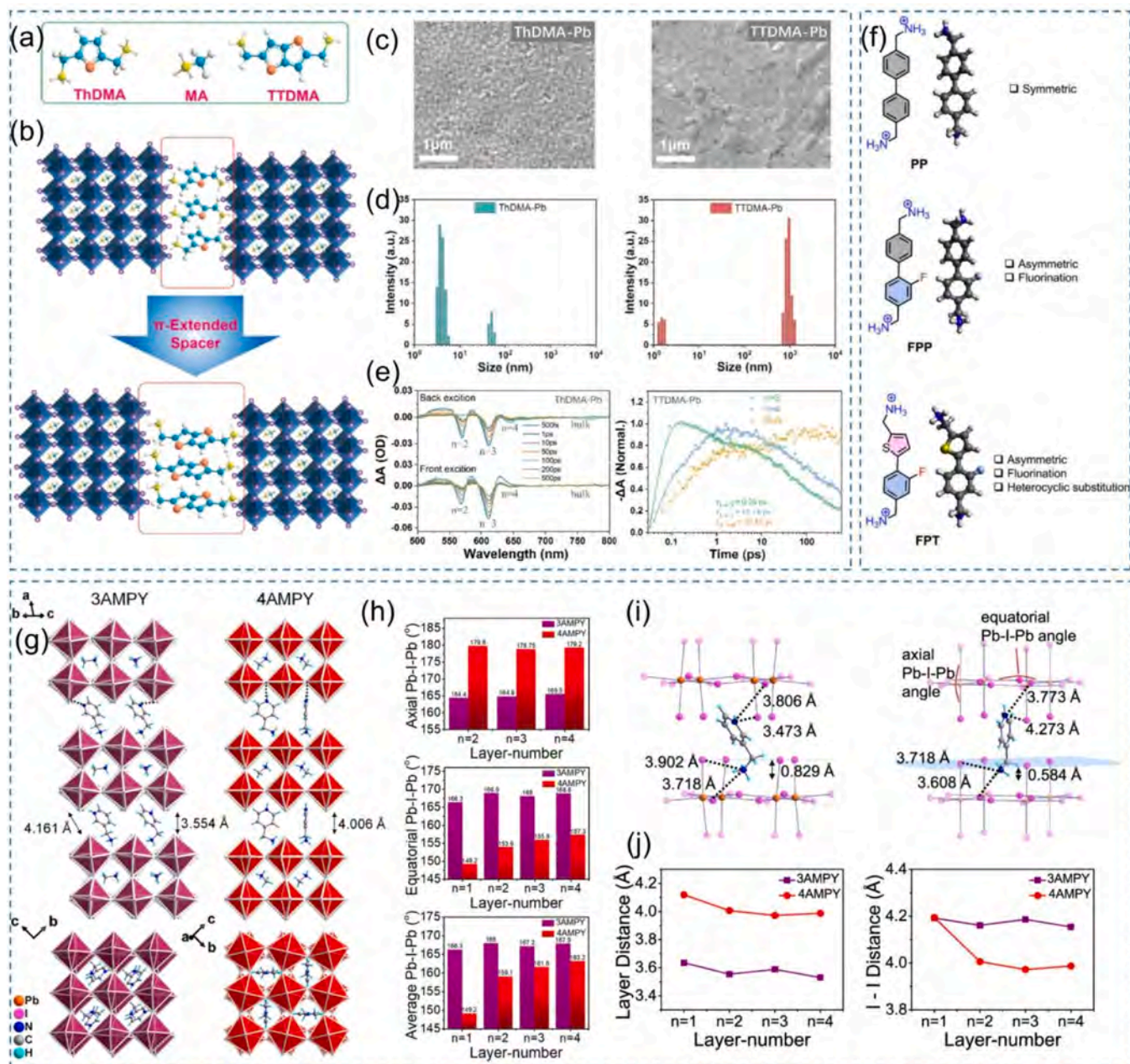
Fig. 10. (a) Chemical structures of MA, ThDMA, and TTDMA spacers. (b) Schematic crystal structures of $(ThDMA)(MA)_{n-1}Pb_nI_{3n+1}$ ($n = 4$, ThDMA-Pb) and $(TTDMA)(MA)_{n-1}Pb_nI_{3n+1}$ ($n = 4$, TTDMA-Pb). (c) Top-view SEM images of ThDMA-Pb and TTDMA-Pb perovskite films. (d) Dynamic light scattering (DLS) spectra of ThDMA-Pb and TTDMA-Pb perovskite precursor solution. (e) TA spectra at selected probe times of ThDMA-Pb and TTDMA-Pb perovskite films. (f) Chemical structures and the optimized molecular conformations for PP, FPP, and FPT. (g) Single crystal structure from the side and top views of $(3AMPY)(MA)Pb_2I_7$ and $(4AMPY)(MA)Pb_2I_7$ perovskite. (h) Average Pb-I-Pb angles for $(xAMPY)(MA)_{n-1}Pb_nI_{3n+1}$ structures ($x = 3$ or 4, $n = 1 - 4$). (i) Comparison for closest NH···I distance of $(3AMPY)(MA)Pb_2I_7$ and $(4AMPY)(MA)Pb_2I_7$ perovskites. (j) Comparison for closest interlayer distance (left) and closest I···I distance (right) of $(3AMPY)(MA)Pb_2I_7$ and $(4AMPY)(MA)Pb_2I_7$ perovskites. (a-e) Reproduced with permission from Ref. [89]. Copyright 2021, Wiley-VCH. (f) Reproduced with permission from Ref. [117]. Copyright 2021, American Chemical Society. (g-j) Reproduced with permission from Ref. [83]. Copyright 2019, American Chemical Society.

3AMPY and 4AMPY-based perovskite structures, which meant the structural disorder gradually weakened. Also, differences in the structures affected the optical properties of DJ perovskites. Finally, the perovskite devices based on 3AMPY spacers with $n = 3$ obtained an outstanding PCE of 9.2 %.

4. Conclusion

In recent years, the importance of 2D perovskites in photovoltaic devices has become increasingly prominent. Compared with traditional 3D perovskites, the advantages of 2D perovskites primarily lie in their

greatly enhanced stability against humidity, heat and light, owing to the introduction of organic hydrophobic ammonium ions. Despite the significant progress in the PCE of 2D perovskites, it generally ranges only from 16 % to 20 %, which is considerably lower than the PCE of over 25 % achieved by 3D perovskites. The reason is that when large organic ammonium ion groups reduce the dimensionality of perovskites from three dimensions to two, it also acts as a "Quantum Well", resulting in a loss in the optoelectronic performance of devices. There are primarily two strategies to address this issue: (1) Enhancing the carrier transport capability in the organic spacer cation layers of 2D perovskites. (2) Inducing the growth of 2D perovskites perpendicular to the substrate

reduces carrier transport in the organic layers and encourages carrier transport in the inorganic octahedral layers as much as possible. However, both approaches require us to identify suitable organic spacer cations for implementation. Recent developments in novel spacer cations have mainly focused on aromatic ammonium ions. Compared to aliphatic spacer cations, aromatic spacer cations have a greater advantage in weakening the influence of quantum confinement effect and improving cross-layer carrier transport ability due to their inherent high dipole moment and aromaticity. The discussion above summarizes the types, characteristics, and impacts on 2D perovskite films and devices of the major aromatic spacer cations reported so far. The difference among aromatic spacer cations is mainly reflected in volume, dipole moment, types and positions of substituents, heterocycles, and conjugate length. Importantly, we think their impact on the performance of perovskite devices is principally manifested through influencing the following characteristics: (a) Quantum barriers: Due to the mismatch in the dielectric constants between the organic and inorganic layers in 2D perovskites, the organic layers can be regarded as a quantum barrier, which restricts the transmission of charges between the inorganic layers. Aromatic spacer cations with high dipole moments have correspondingly larger dielectric constants, which can reduce the impact of the quantum barrier and enhance the interlayer charge transfer capability. (b) Film quality: Appropriate aromatic spacer cations can induce 2D perovskite films to grow in the preferred perpendicular orientation to the substrate, thereby reducing charge transfer between the organic and inorganic layers and enhancing out-of-plane charge transfer capability. High-quality films with fewer grain boundaries and larger grains can also enhance the performance of the corresponding devices. (c) Phase distribution: Phases with different n values typically coexist in 2D perovskite films. Aromatic spacer cations such as F-PEA and PEA, which can induce the formation of an orderly arranged n-phase distribution from low to high, are more beneficial for separating and transporting excitons. (d) Humidity stability: How well the aromatic spacer ions can repel water molecules is strongly related to the stability of the 2D perovskites. (e) Interactions between the organic and inorganic layers: Different aromatic spacer cations have different levels of interaction with the inorganic octahedra. Stronger interaction can better stabilize the perovskite structure. (f) Interactions between the organic layers: For 2D RP-type perovskites, the organic layer contains two layers of ammonium ions. Different ammonium ions can lead to different interlayer stacking modes of ammonium ions. Generally speaking, face-to-face stacking is more beneficial to the performance of perovskites.

Considering the impact of all these aspects is crucial for selecting or designing aromatic spacer cations. Overall, suitable aromatic spacer cations always exhibit the following characteristics: high dielectric constant, high hydrophobicity, appropriate volume, long conjugated length, and ability to strongly interact with the inorganic octahedral layers and organic spacer layers (only for RP-type) in perovskite lattices. However, incorporating all these characteristics into a single aromatic spacer cation is often difficult. Therefore, making appropriate trade-offs or employing a variety of spacer cations is often necessary.

As we discussed above, the development of aromatic spacer cations can be mainly divided into four directions: (1) modification of alkyl chains, (2) replacement of hydrogen atoms on the aromatic ring with specific substituents, (3) substitution of benzene rings with aromatic heterocycles, and (4) replacement of a monoaromatic ring with multiple aromatic rings. If we think about it carefully, we can notice that although changes in spacers structure always lead to multiple effects on 2D perovskites, every direction of modifying or designing spacers possess its unique advantage and impact. For example, the effect of modified alkyl chains of spacers is mainly manifested in changing the interaction between the spacers and the inorganic octahedral sheets. That always makes a difference in stability of perovskites. Introducing specific substituent group on the aromatic ring gives us the freedom to adjust the dipole moment of spacers and different substituent group can lead to different stacking mode of inorganic layers and phases

distribution in 2D perovskites. And multiple aromatic ring spacers have greater advantages in weakening or even breaking the quantum confinement effect. It may be possible that the future design of spacer cations can combine these design directions.

Indeed, designing new aromatic spacers to achieve higher PCE for 2D perovskite is promising, but there are also huge challenges in design and synthesis of spacers. However, based on the above discussion, we believe that in the future, the device performance of 2D perovskites could rival or even surpass that of 3D perovskites.

CRediT authorship contribution statement

Yi Shen: Writing – original draft, Project administration, Formal analysis, Conceptualization. **Siliang Hu:** Writing – original draft, Investigation. **You Meng:** Formal analysis. **SenPo Yip:** Writing – review & editing. **Johnny C. Ho:** Writing – review & editing, Writing – original draft, Funding acquisition.

Declaration of competing interest

The authors declare that they have no known competing financial interests or personal relationships that could have appeared to influence the work reported in this paper.

Data availability

No data was used for the research described in the article.

Acknowledgment

Supplementary materials

Supplementary material associated with this article can be found, in the online version, at doi:10.1016/j.mtelec.2024.100100.

References

[1] B.K. Singh, M. Delgado-Baquerizo, E. Egidi, E. Guirado, J.E. Leach, H. Liu, P. Trivedi, Climate change impacts on plant pathogens, food security and paths forward, Nat. Rev. Microbiol. 21 (2023) 640–656, https://doi.org/10.1038/s41579-023-00900-7.

[2] K. Zheng, T. Pullerits, Two dimensions are better for perovskites, J. Phys. Chem. Lett. 10 (2019) 5881–5885, https://doi.org/10.1021/acs.jpclett.9b01568.

[3] M.A. Green, A. Ho-Baillie, H.J. Snaith, The emergence of perovskite solar cells, Nat. Photonics. 8 (2014) 506–514, https://doi.org/10.1038/nphoton.2014.134.

[4] H.P. Wang, S.Y. Li, X.Y. Liu, Z.F. Shi, X.S. Fang, J.H. He, Low-dimensional metal halide perovskite photodetectors, Adv. Mater. 33 (2021) 2003309, https://doi.org/10.1002/adma.202003309.

[5] A. Krishna, S. Gottis, M.K. Nazeeruddin, F. Sauvage, Mixed dimensional 2D/3D hybrid perovskite absorbers: the future of perovskite solar cells? Adv. Funct. Mater. 29 (2018) https://doi.org/10.1002/adfm.201806482.

[6] J. Liang, X. Hu, C. Wang, C. Liang, C. Chen, M. Xiao, J. Li, C. Tao, G. Xing, R. Yu, W. Ke, G. Fang, Origins and influences of metallic lead in perovskite solar cells, Joule 6 (2022) 816–833, https://doi.org/10.1016/j.joule.2022.03.005.

[7] Q. Jiang, J. Tong, Y. Xian, R.A. Kerner, S.P. Dunfield, C. Xiao, R.A. Scheidt, D. Kuciauskas, X. Wang, M.P. Hautzinger, R. Tirawat, M.C. Beard, D.P. Fenning, J.J. Berry, B.W. Larson, Y. Yan, K. Zhu, Surface reaction for efficient and stable inverted perovskite solar cells, Nature 611 (2022) 278–283, https://doi.org/10.1038/s41586-022-05268-x.

[8] H. Min, D.Y. Lee, J. Kim, G. Kim, K.S. Lee, J. Kim, M.J. Paik, Y.K. Kim, K.S. Kim, M.G. Kim, T.J. Shin, S. Il Seok, *Perovskite solar cells with atomically coherent interlayers on* SnO$_{(2)}$electrodes, Nature 598 (2021) 444–450, https://doi.org/10.1038/s41586-021-03964-8.

[9] A. Miyata, A. Mitioglu, P. Plochocka, O. Portugall, J.T.W. Wang, S.D. Stranks, H.J. Snaith, R.J. Nicholas, Direct measurement of the exciton binding energy and effective masses for charge carriers in organic–inorganic tri-halide perovskites, Nat. Phys. 11 (2015) 582–587, https://doi.org/10.1038/nphys3357.

[10] L.K. Ono, Y. Qi, S. Liu, Progress toward stable lead halide perovskite solar cells, Joule 2 (2018) 1961–1990, https://doi.org/10.1016/j.joule.2018.07.007.

[11] A. Ren, H. Lai, X. Hao, Z. Tang, H. Xu, B.M.F. Wu Jeco, K. Watanabe, L. Wu, J. Zhang, M. Sugiyama, J. Wu, D. Zhao, Efficient perovskite solar modules with minimized nonradiative recombination and local carrier transport losses, Joule 4 (2020) 1263–1277, https://doi.org/10.1016/j.joule.2020.04.013.

[12] C. Wang, Y. Zhao, T. Ma, Y. An, R. He, J. Zhu, C. Chen, S. Ren, F. Fu, D. Zhao, X. Li, A universal close-space annealing strategy towards high-quality perovskite absorbers enabling efficient all-perovskite tandem solar cells, Nat. Energy. 7 (2022) 744–753, https://doi.org/10.1038/s41560-022-01076-9.

[13] C. Liu, M. Chen, H. Zhou, H. Lu, Y. Yang, Efficient carrier generation and transport of $CsPb_{1-x}Mn_x(Br/Cl)_3$ quantum dots in high-performance carbon-based perovskite solar cells, Appl. Phys. A 128 (2022), https://doi.org/10.1007/s00339-022-06196-3.

[14] M. Zhang, W. Li, W. Zhao, X. Han, Enhancing charge carrier transport in the carbon-electrode-based $CsPbI_2Br$ perovskite solar cells via i/br homogenization process modulation and oleic acid surface passivation, ACS Appl. Energy Materials. 6 (2023) 2973–2980, https://doi.org/10.1021/acsaem.2c04019.

[15] Y. Zhang, L. Xu, J. Sun, Y. Wu, Z. Kan, H. Zhang, L. Yang, B. Liu, B. Dong, X. Bai, H. Song, 24.11% high performance perovskite solar cells by dual interfacial carrier mobility enhancement and charge-carrier transport balance, Adv. Energy Mater. 12 (2022), https://doi.org/10.1002/aenm.202201269.

[16] M.A. Green, Y. Jiang, A.M. Soufiani, A. Ho-Baillie, Optical properties of photovoltaic organic-inorganic lead halide perovskites, J. Phys. Chem. Lett. 6 (2015) 4774–4785, https://doi.org/10.1021/acs.jpclett.5b01865.

[17] M. Saba, F. Quochi, A. Mura, G. Bongiovanni, Excited state properties of hybrid perovskites, Acc. Chem. Res. 49 (2016) 166–173, https://doi.org/10.1021/acs.accounts.5b00445.

[18] E.L. Unger, L. Kegelmann, K. Suchan, D. Sörell, L. Korte, S. Albrecht, Roadmap and roadblocks for the band gap tunability of metal halide perovskites, J. Mater. Chem. A. 5 (2017) 11401–11409, https://doi.org/10.1039/c7ta00404d.

[19] K. Ema, K. Umeda, M. Toda, C. Yajima, Y. Arai, H. Kunugita, D. Wolverson, J. J. Davies, Huge exchange energy and fine structure of excitons in an organic-inorganic quantum well material, Phy. Rev. B. 73 (2006), https://doi.org/10.1103/PhysRevB.73.241310.

[20] S.B. Zhang, S-HW, and Alex Zunger, Stabilization of ternary compounds via ordered arrays of defect pairs. Phys. Rev. Lett. 78 (1997), doi:10.1103/PhysRevLett.78.4059.

[21] J.M. Ball, M.M. Lee, A. Hey, H.J. Snaith, Low-temperature processed meso-superstructured to thin-film perovskite solar cells, Energy Enviro. Sci. 6 (2013), https://doi.org/10.1039/c3ee40810h.

[22] J. Burschka, N. Pellet, S.J. Moon, R. Humphry-Baker, P. Gao, M.K. Nazeeruddin, M. Gratzel, Sequential deposition as a route to high-performance perovskite-sensitized solar cells, Nature 499 (2013) 316–319, https://doi.org/10.1038/nature12340.

[23] N.J. Jeon, J.H. Noh, Y.C. Kim, W.S. Yang, S. Ryu, S.I. Seok, Solvent engineering for high-performance inorganic-organic hybrid perovskite solar cells, Nat. Mater. 13 (2014) 897–903, https://doi.org/10.1038/nmat4014.

[24] J.J. Yoo, G. Seo, M.R. Chua, T.G. Park, Y. Lu, F. Rotermund, Y.K. Kim, C.S. Moon, N.J. Jeon, J.P. Correa-Baena, V. Bulovic, S.S. Shin, M.G. Bawendi, J. Seo, Efficient perovskite solar cells via improved carrier management, Nature 590 (2021) 587–593, https://doi.org/10.1038/s41586-021-03285-w.

[25] Y. Wang, T. Gould, J.F. Dobson, H. Zhang, H. Yang, X. Yao, H. Zhao, Density functional theory analysis of structural and electronic properties of orthorhombic perovskite $CH_3NH_3PbI_3$, Phys. Chem. Chem. Phys. 16 (2014) 1424–1429, https://doi.org/10.1039/c3cp54479f.

[26] H. Zhang, X. Fu, Y. Tang, H. Wang, C. Zhang, W.W. Yu, X. Wang, Y. Zhang, M. Xiao, Phase segregation due to ion migration in all-inorganic mixed-halide perovskite nanocrystals, Nat. Commun. 10 (2019) 1088, https://doi.org/10.1038/s41467-019-09047-7.

[27] T. Leijtens, G.E. Eperon, N.K. Noel, S.N. Habisreutinger, A. Petrozza, H.J. Snaith, Stability of metal halide perovskite solar cells, Adv. Energy Mater. 5 (2015), https://doi.org/10.1002/aenm.201500963.

[28] K. Miyano, M. Yanagida, N. Tripathi, Y. Shirai, Hysteresis, stability, and ion migration in lead halide perovskite photovoltaics, J. Phys. Chem. Lett. 7 (2016) 2240–2245, https://doi.org/10.1021/acs.jpclett.6b00579.

[29] H. Chen, F. Zhou, Z. Jin, *Interface engineering, the trump-card for CsPbX₃(X=I, Br) perovskite solar cells development,* Nano Energy 79 (2021), https://doi.org/10.1016/j.nanoen.2020.105490.

[30] T.H. Han, S. Tan, J. Xue, L. Meng, J.W. Lee, Y. Yang, Interface and defect engineering for metal halide perovskite optoelectronic devices, Adv. Mater. 31 (2019) e1803515, https://doi.org/10.1002/adma.201803515.

[31] W. Yu, S. Sun, M. Xiao, T. Hou, X. Liu, B. Zheng, H. Yu, M. Zhang, Y. Huang, X. Hao, Recent advances on interface engineering of perovskite solar cells, Nano Res. 15 (2021) 85–103, https://doi.org/10.1007/s12274-021-3488-7.

[32] G. Wu, R. Liang, M. Ge, G. Sun, Y. Zhang, G. Xing, Surface passivation using 2D perovskites toward efficient and stable perovskite solar cells, Adv. Mater. 34 (2022) e2105635, https://doi.org/10.1002/adma.202105635.

[33] Y. Han, H. Zhao, C. Duan, S. Yang, Z. Yang, Z. Liu, S. Liu, *Controlled n-doping in air-stable $CsPbI_2Br$ perovskite solar cells with a record efficiency of 16.79%,* Adv. Funct. Mater. 30 (2020) https://doi.org/10.1002/adfm.201909972.

[34] Y. Zhou, Z. Zhou, M. Chen, Y. Zong, J. Huang, S. Pang, N.P. Padture, Doping and alloying for improved perovskite solar cells, J. Mater. Chem. A. 4 (2016) 17623–17635, https://doi.org/10.1039/c6ta08699c.

[35] J. Yuan, B. Li, C. Hao, Study on cobalt doped tin based perovskite material with enhanced air stability, Mater. Sci. Semicond. Process 57 (2017) 95–98, https://doi.org/10.1016/j.mssp.2016.09.029.

[36] Z. Fu, M. Xu, Y. Sheng, Z. Yan, J. Meng, C. Tong, D. Li, Z. Wan, Y. Ming, A. Mei, Y. Hu, Y. Rong, H. Han, Encapsulation of printable mesoscopic perovskite solar cells enables high temperature and long-term outdoor stability, Adv. Funct. Mater. 29 (2019), https://doi.org/10.1002/adfm.201809129.

[37] F. Matteocci, L. Cinà, E. Lamanna, S. Cacovich, G. Divitini, P.A. Midgley, C. Ducati, A. Di Carlo, Encapsulation for long-term stability enhancement of perovskite solar cells, Nano Energy 30 (2016) 162–172, https://doi.org/10.1016/j.nanoen.2016.09.041.

[38] D. Li, Z. Xing, X. Meng, X. Hu, T. Hu, Y. Chen, Spontaneous internal encapsulation via dual interfacial perovskite heterojunction enables highly efficient and stable perovskite solar cells, Nano Lett. 23 (2023) 3484–3492, https://doi.org/10.1021/acs.nanolett.3c00486.

[39] H.C. Weerasinghe, Y. Dkhissi, A.D. Scully, R.A. Caruso, Y.B. Cheng, Encapsulation for improving the lifetime of flexible perovskite solar cells, Nano Energy 18 (2015) 118–125, https://doi.org/10.1016/j.nanoen.2015.10.006.

[40] C. Liang, H. Gu, Y. Xia, Z. Wang, X. Liu, J. Xia, S. Zuo, Y. Hu, X. Gao, W. Hui, L. Chao, T. Niu, M. Fang, H. Lu, H. Dong, H. Yu, S. Chen, X. Ran, L. Song, B. Li, J. Zhang, Y. Peng, G. Shao, J. Wang, Y. Chen, G. Xing, W. Huang, Two-dimensional Ruddlesden–Popper layered perovskite solar cells based on phase-pure thin films, Nat. Energy. 6 (2020) 38–45, https://doi.org/10.1038/s41560-020-00721-5.

[41] I.C. Smith, E.T. Hoke, D. Solis-Ibarra, M.D. McGehee, H.I. Karunadasa, A layered hybrid perovskite solar-cell absorber with enhanced moisture stability, Angew. Chem. Int. Ed. Engl. 53 (2014) 11232–11235, https://doi.org/10.1002/anie.201406466.

[42] G. Wu, T. Yang, X. Li, N. Ahmad, X. Zhang, S. Yue, J. Zhou, Y. Li, H. Wang, X. Shi, S. Liu, K. Zhao, H. Zhou, Y. Zhang, Molecular engineering for two-dimensional perovskites with photovoltaic efficiency exceeding 18%, Matter. 4 (2021) 582–599, https://doi.org/10.1016/j.matt.2020.11.011.

[43] J. Xu, J. Chen, S. Chen, H. Gao, Y. Li, Z. Jiang, Y. Zhang, X. Wang, X. Zhu, B. Xu, Organic spacer engineering of Ruddlesden-Popper perovskite materials toward efficient and stable solar cells, Chem. Eng. J. 453 (2023), https://doi.org/10.1016/j.cej.2022.139790.

[44] F. Ledee, P. Audebert, G. Trippe-Allard, L. Galmiche, D. Garrot, J. Marrot, J. S. Lauret, E. Deleporte, C. Katan, J. Even, C. Quarti, Tetrazine molecules as an efficient electronic diversion channel in 2D organic-inorganic perovskites, Mater. Horiz. 8 (2021) 1547–1560, https://doi.org/10.1039/d0mh01904f.

[45] J.T. Lin, D.G. Chen, C.H. Wu, C.S. Hsu, C.Y. Chien, H.M. Chen, P.T. Chou, C. W. Chiu, A universal approach for controllable synthesis of n-specific layered 2d perovskite nanoplates, Angew. Chem. Int. Ed. Engl. 60 (2021) 7866–7872, https://doi.org/10.1002/anie.202016140.

[46] H. Pan, X. Zhao, X. Gong, Y. Shen, M. Wang, Atomic-scale tailoring of organic cation of layered ruddlesden-popper perovskite compounds, J. Phys. Chem. Lett. 10 (2019) 1813–1819, https://doi.org/10.1021/acs.jpclett.9b00479.

[47] W.T.M. Van Gompel, R. Herckens, P.H. Denis, M. Mertens, M.C. Gélvez-Rueda, K. Van Hecke, B. Ruttens, J. D'Haen, F.C. Grozema, L. Lutsen, D. Vanderzande, 2D layered perovskite containing functionalised benzothieno-benzothiophene molecules: formation, degradation, optical properties and photoconductivity, J. Mater. Chem. C. 8 (2020) 7181–7188, https://doi.org/10.1039/d0tc01053g.

[48] Z. Wang, X. Liu, H. Ren, L. Liu, X. Tang, X. Yao, Z. Su, X. Gao, Q. Wei, H. Xie, Y. Zheng, M. Li, Insight into the enhanced charge transport in quasi-2D perovskite via fluorination of ammonium cations for photovoltaic applications, ACS Appl. Mater. Interfaces. 14 (2022) 7917–7925, https://doi.org/10.1021/acsami.1c21715.

[49] X. Hong, T. Ishihara, A.V. Nurmikko, Dielectric confinement effect on excitons in PbI4-based layered semiconductors, Phys. Rev. B Condens. Matter. 45 (1992) 6961–6964, https://doi.org/10.1103/physrevb.45.6961.

[50] E.A. Muljarov, S.G. Tikhodeev, N.A. Gippius, T. Ishihara, Excitons in self-organized semiconductor/insulator superlattices: pbI-based perovskite compounds, Phys. Rev. B Condens. Matter. 51 (1995) 14370–14378, https://doi.org/10.1103/physrevb.51.14370.

[51] J.M. Hoffman, X. Che, S. Sidhik, X. Li, I. Hadar, J.C. Blancon, H. Yamaguchi, M. Kepenekian, C. Katan, J. Even, C.C. Stoumpos, A.D. Mohite, M.G. Kanatzidis, From 2D to 1D electronic dimensionality in halide perovskites with stepped and flat layers using propylammonium as a spacer, J. Am. Chem. Soc. 141 (2019) 10661–10676, https://doi.org/10.1021/jacs.9b02846.

[52] C. Ma, D. Shen, T.W. Ng, M.F. Lo, C.S. Lee, 2D Perovskites with short interlayer distance for high-performance solar cell application, Adv. Mater. 30 (2018) e1800710, https://doi.org/10.1002/adma.201800710.

[53] C.C. Stoumpos, D.H. Cao, D.J. Clark, J. Young, J.M. Rondinelli, J.I. Jang, J. T. Hupp, M.G. Kanatzidis, Ruddlesden–popper hybrid lead iodide perovskite 2d homologous semiconductors, Chem. Mater. 28 (2016) 2852–2867, https://doi.org/10.1021/acs.chemmater.6b00847.

[54] D.H. Cao, C.C. Stoumpos, O.K. Farha, J.T. Hupp, M.G. Kanatzidis, 2D homologous perovskites as light-absorbing materials for solar cell applications, J. Am. Chem. Soc. 137 (2015) 7843–7850, https://doi.org/10.1021/jacs.5b03796.

[55] Y. Chen, Y. Sun, J. Peng, W. Zhang, X. Su, K. Zheng, T. Pullerits, Z. Liang, Tailoring organic cation of 2D air-stable organometal halide perovskites for highly efficient planar solar cells, Adv. Energy Mater. 7 (2017), https://doi.org/10.1002/aenm.201700162.

[56] J.M. Hoffman, C.D. Malliakas, S. Sidhik, I. Hadar, R. McClain, A.D. Mohite, M. G. Kanatzidis, Long periodic ripple in a 2D hybrid halide perovskite structure

using branched organic spacers, Chem. Sci. 11 (2020) 12139–12148, https://doi.org/10.1039/d0sc04144k.

[57] M.E. Kamminga, H.H. Fang, M.R. Filip, F. Giustino, J. Baas, G.R. Blake, M.A. Loi, T.T.M. Palstra, Confinement effects in low-dimensional lead iodide perovskite hybrids, Chem. Mater. 28 (2016) 4554–4562, https://doi.org/10.1021/acs.chemmater.6b00809.

[58] H. Lai, B. Kan, T. Liu, N. Zheng, Z. Xie, T. Zhou, X. Wan, X. Zhang, Y. Liu, Y. Chen, Two-dimensional ruddlesden–popper perovskite with nanorod-like morphology for solar cells with efficiency exceeding 15%, J. Am. Chem. Soc. 140 (2018) 11639–11646, https://doi.org/10.1021/jacs.8b04604.

[59] S. Ahmad, P. Fu, S. Yu, Q. Yang, X. Liu, X. Wang, X. Wang, X. Guo, C. Li, Dion-jacobson phase 2D layered perovskites for solar cells with ultrahigh stability, Joule 3 (2019) 794–806, https://doi.org/10.1016/j.joule.2018.11.026.

[60] X. Li, J. Hoffman, W. Ke, M. Chen, H. Tsai, W. Nie, A.D. Mohite, M. Kepenekian, C. Katan, J. Even, M.R. Wasielewski, C.C. Stoumpos, M.G. Kanatzidis, *Two-dimensional halide perovskites incorporating straight chain symmetric diammonium ions, (NH(3)C(m)H(2m)NH(3))(CH(3)NH(3))(n-1)Pb(n)I(3 n+1) (m = 4-9; n = 1-4)*, J. Am. Chem. Soc. 140 (2018) 12226–12238, https://doi.org/10.1021/jacs.8b07712.

[61] Y. Li, J.V. Milic, A. Ummadisingu, J.Y. Seo, J.H. Im, H.S. Kim, Y. Liu, M.I. Dar, S.M. Zakeeruddin, P. Wang, A. Hagfeldt, M. Gratzel, Bifunctional organic spacers for formamidinium-based hybrid dion-jacobson two-dimensional perovskite solar cells, Nano Lett. 19 (2019) 150–157, https://doi.org/10.1021/acs.nanolett.8b03552.

[62] J. Shi, Y. Gao, X. Gao, Y. Zhang, J. Zhang, X. Jing, M. Shao, Fluorinated low-dimensional ruddlesden-popper perovskite solar cells with over 17% power conversion efficiency and improved stability, Adv. Mater. 31 (2019) e1901673, https://doi.org/10.1002/adma.201901673.

[63] W. Fu, J. Wang, L. Zuo, K. Gao, F. Liu, D.S. Ginger, A.K.Y. Jen, Two-dimensional perovskite solar cells with 14.1% power conversion efficiency and 0.68% external radiative efficiency, ACS. Energy Lett. 3 (2018) 2086–2093, https://doi.org/10.1021/acsenergylett.8b01181.

[64] Y. Yan, S. Yu, A. Honarfar, T. Pullerits, K. Zheng, Z. Liang, Benefiting from spontaneously generated 2D/3D bulk-heterojunctions in ruddlesden-popper perovskite by incorporation of S-bearing spacer cation, Adv. Sci. (Weinh) 6 (2019) 1900548, https://doi.org/10.1002/advs.201900548.

[65] Z. Li, N. Liu, K. Meng, Z. Liu, Y. Hu, Q. Xu, X. Wang, S. Li, L. Cheng, G. Chen, A new organic interlayer spacer for stable and efficient 2D ruddlesden–popper perovskite solar cells, Nano Lett. 19 (2019) 5237–5245, https://doi.org/10.1021/acs.nanolett.9b01652.

[66] Y. Li, H. Cheng, K. Zhao, Z.S. Wang, 4-(Aminoethyl)pyridine as a bifunctional spacer cation for efficient and STable 2D ruddlesden-popper perovskite solar cells, ACS. Appl. Mater. Interfaces. 11 (2019) 37804–37811, https://doi.org/10.1021/acsami.9b13951.

[67] Q. Li, Y. Dong, G. Lv, T. Liu, D. Lu, N. Zheng, X. Dong, Z. Xu, Z. Xie, Y. Liu, Fluorinated aromatic formamidinium spacers boost efficiency of layered ruddlesden–popper perovskite solar cells, ACS. Energy Lett. 6 (2021) 2072–2080, https://doi.org/10.1021/acsenergylett.1c00620.

[68] R. Liu, C. Liu, Y. Yu, H. Yu, X. Xu, Aromatic heterocyclic organic spacer cation-assisted growth of large-grain-size 2DRP perovskite film for enhanced solar cell performance, J. Phys. Chem. Lett. 13 (2022) 8945–8952, https://doi.org/10.1021/acs.jpclett.2c01612.

[69] C. Ran, W. Gao, J. Li, J. Xi, L. Li, J. Dai, Y. Yang, X. Gao, H. Dong, B. Jiao, I. Spanopoulos, C.D. Malliakas, X. Hou, M.G. Kanatzidis, Z. Wu, Conjugated organic cations enable efficient self-healing FASnI3 solar cells, Joule 3 (2019) 3072–3087, https://doi.org/10.1016/j.joule.2019.08.023.

[70] Z. Xu, L. Li, X. Dong, D. Lu, R. Wang, W.J. Yin, Y. Liu, CsPbI(3)-Based phase-stable 2D ruddlesden-popper perovskites for efficient solar cells, Nano Lett. 22 (2022) 2874–2880, https://doi.org/10.1021/acs.nanolett.2c00002.

[71] G. Yang, G. Sui, W. Chen, K. Su, Y. Feng, B. Zhang, Selectively fluorinated benzylammonium-based spacer cation enables graded quasi-2D perovskites for efficient and stable solar cells, Chem. Mater. 34 (2022) 3346–3356, https://doi.org/10.1021/acs.chemmater.2c00146.

[72] Q. Fu, M. Chen, Q. Li, H. Liu, R. Wang, Y. Liu, Selenophene-based 2D ruddlesden-popper perovskite solar cells with an efficiency exceeding 19, J. Am. Chem. Soc. 145 (2023) 21687–21695, https://doi.org/10.1021/jacs.3c08604.

[73] Z. Xu, D. Lu, F. Liu, H. Lai, X. Wan, X. Zhang, Y. Liu, Y. Chen, Phase distribution and carrier dynamics in multiple-ring aromatic spacer-based two-dimensional Ruddlesden-popper perovskite solar cells, ACS. Nano 14 (2020) 4871–4881, https://doi.org/10.1021/acsnano.0c00875.

[74] R. Wang, X. Dong, Q. Ling, Q. Fu, Z. Hu, Z. Xu, H. Zhang, Q. Li, Y. Liu, Spacer engineering for 2d Ruddlesden–popper perovskites with an Ultralong carrier lifetime of over 18 μs enable efficient solar cells, ACS. Energy Lett. 7 (2022) 3656–3665, https://doi.org/10.1021/acsenergylett.2c01800.

[75] R. Yang, R. Li, Y. Cao, Y. Wei, Y. Miao, W.L. Tan, X. Jiao, H. Chen, L. Zhang, Q. Chen, H. Zhang, W. Zou, Y. Wang, M. Yang, C. Yi, N. Wang, F. Gao, C. R. McNeill, T. Qin, J. Wang, W. Huang, Oriented quasi-2D perovskites for high performance optoelectronic devices, Adv. Mater. 30 (2018) https://doi.org/10.1002/adma.201804771.

[76] J. Yang, T. He, M. Li, G. Li, H. Liu, J. Xu, M. Zhang, W. Zuo, R. Qin, M. H. Aldamasy, M. Yuan, Z. Li, M. Malekshahi Byranvand, M. Saliba, A. Abate, π-Conjugated carbazole cations enable wet-stable quasi-2D perovskite photovoltaics, ACS. Energy Lett. 7 (2022) 4451–4458, https://doi.org/10.1021/acsenergylett.2c02219.

[77] X. Dong, M. Chen, R. Wang, Q. Ling, Z. Hu, H. Liu, Y. Xin, Y. Yang, J. Wang, Y. Liu, Quantum confinement breaking: orbital coupling in 2d

[78] Ruddlesden–popper perovskites enables efficient solar cells, Adv. Energy Mater. 13 (2023), https://doi.org/10.1002/aenm.202301006.

[78] Y. Zhang, M. Chen, T. He, H. Chen, Z. Zhang, H. Wang, H. Lu, Q. Ling, Z. Hu, Y. Liu, Y. Chen, G. Long, Highly efficient and stable FA-based quasi-2D Ruddlesden-popper perovskite solar cells by the incorporation of beta-fluorophenylethanamine cations, Adv. Mater. 35 (2023) e2210836, https://doi.org/10.1002/adma.202210836.

[79] R. Wang, X. Dong, Q. Ling, Z. Hu, Y. Gao, Y. Chen, Y. Liu, Nucleation and crystallization in 2D Ruddlesden-popper perovskites using formamidinium-based organic semiconductor spacers for efficient solar cells, Angew. Chem. Int. Ed. Engl. 62 (2023) e202314690, https://doi.org/10.1002/anie.202314690.

[80] F. Zhang, D.H. Kim, H. Lu, J.S. Park, B.W. Larson, J. Hu, L. Gao, C. Xiao, O. G. Reid, X. Chen, Q. Zhao, P.F. Ndione, J.J. Berry, W. You, A. Walsh, M.C. Beard, K. Zhu, Enhanced charge transport in 2D perovskites via fluorination of organic cation, J. Am. Chem. Soc. 141 (2019) 5972–5979, https://doi.org/10.1021/jacs.9b00972.

[81] Z. Wang, Q. Wei, X. Liu, L. Liu, X. Tang, J. Guo, S. Ren, G. Xing, D. Zhao, Y. Zheng, Spacer cation tuning enables vertically oriented and graded quasi-2d perovskites for efficient solar cells, Adv. Funct. Mater. 31 (2020), https://doi.org/10.1002/adfm.202008404.

[82] M. Shao, T. Bie, L. Yang, Y. Gao, X. Jin, F. He, N. Zheng, Y. Yu, X. Zhang, Over 21% efficiency STable 2D perovskite solar cells, Adv. Mater. 34 (2022) e2107211, https://doi.org/10.1002/adma.202107211.

[83] X. Li, W. Ke, B. Traore, P. Guo, I. Hadar, M. Kepenekian, J. Even, C. Katan, C. C. Stoumpos, R.D. Schaller, M.G. Kanatzidis, Two-dimensional dion-jacobson hybrid lead iodide perovskites with aromatic diammonium cations, J. Am. Chem. Soc. 141 (2019) 12880–12890, https://doi.org/10.1021/jacs.9b06398.

[84] S. Yu, S. Yan, M. Abdellah, T. Pullerits, K. Zheng, Z. Liang, Nonconfinement structure revealed in dion-jacobson type quasi-2D perovskite expedites interlayer charge transport, Small. 15 (2019) e1905081, https://doi.org/10.1002/smll.201905081.

[85] X. Zhang, T. Yang, X. Ren, L. Zhang, K. Zhao, S. Liu, Film formation control for high performance Dion–jacobson 2D perovskite solar cells, Adv. Energy Mater. 11 (2021), https://doi.org/10.1002/aenm.202002733.

[86] R.D.Chavan Yukta, D. Prochowicz, P. Yadav, M.M. Tavakoli, S. Satapathi, Thiocyanate-passivated diaminonaphthalene-incorporated dion–jacobson perovskite for highly efficient and stable solar cells, Acs Appl Mater Inter 14 (2022) 850–860, https://doi.org/10.1021/acsami.1c19546.

[87] D. Wang, S.C. Chen, Q. Zheng, Enhancing the efficiency and stability of two-dimensional Dion–Jacobson perovskite solar cells using a fluorinated diammonium spacer, J. Mater. Chem. A. 9 (2021) 11778–11786, https://doi.org/10.1039/d1ta01447a.

[88] G. Lv, L. Li, D. Lu, Z. Xu, Y. Dong, Q. Li, Z. Chang, W.J. Yin, Y. Liu, Multiple-noncovalent-interaction-stabilized layered dion-jacobson perovskite for efficient solar cells, Nano Lett. 21 (2021) 5788–5797, https://doi.org/10.1021/acs.nanolett.1c01505.

[89] D. Lu, G. Lv, Z. Xu, Y. Dong, X. Ji, Y. Liu, Thiophene-based two-dimensional dion-jacobson perovskite solar cells with over 15% efficiency, J. Am. Chem. Soc. 142 (2020) 11114–11122, https://doi.org/10.1021/jacs.0c03363.

[90] Y. Dong, X. Dong, D. Lu, M. Chen, N. Zheng, R. Wang, Q. Li, Z. Xie, Y. Liu, Orbital interactions between the organic semiconductor spacer and the inorganic layer in dion-jacobson perovskites enable efficient solar cells, Adv. Mater. 35 (2023) e2205258, https://doi.org/10.1002/adma.202205258.

[91] Z. Xu, D. Lu, X. Dong, M. Chen, Q. Fu, Y. Liu, Highly efficient and stable dion-jacobson perovskite solar cells enabled by extended pi-conjugation of organic spacer, Adv. Mater. 33 (2021) e2105083, https://doi.org/10.1002/adma.202105083.

[92] J. Xi, I. Spanopoulos, K. Bang, J. Xu, H. Dong, Y. Yang, C.D. Malliakas, J. M. Hoffman, M.G. Kanatzidis, Z. Wu, Alternative organic spacers for more efficient perovskite solar cells containing ruddlesden-popper phases, J. Am. Chem. Soc. 142 (2020) 19705–19714, https://doi.org/10.1021/jacs.0c09647.

[93] J. Rodríguez-Romero, J. Sanchez-Diaz, C. Echeverría-Arrondo, S. Masi, D. Esparza, E.M. Barea, I. Mora-Seró, Widening the 2D/3D perovskite family for efficient and thermal-resistant solar cells by the use of secondary ammonium cations, ACS. Energy Lett. 5 (2020) 1013–1021, https://doi.org/10.1021/acsenergylett.9b02755.

[94] S. Song, S.J. Yang, J. Choi, S.G. Han, K. Park, H. Lee, J. Min, S. Ryu, K. Cho, Surface stabilization of a formamidinium perovskite solar cell using quaternary ammonium salt, Acs Appl Mater Inter 13 (2021) 37052–37062, https://doi.org/10.1021/acsami.1c07690.

[95] H. Xu, Z. Liang, J. Ye, Y. Zhang, Z. Wang, H. Zhang, C. Wan, G. Xu, J. Zeng, B. Xu, Z. Xiao, T. Kirchartz, X. Pan, Constructing robust heterointerfaces for carrier viaduct via interfacial molecular bridges enables efficient and stable inverted perovskite solar cells, Energy Environ. Mater. 16 (2023) 5792–5804, https://doi.org/10.1039/d3ee02591h.

[96] Y. Dong, D. Lu, Z. Xu, H. Lai, Y. Liu, 2-Thiopheneformamidinium-based 2D Ruddlesden–popper perovskite solar cells with efficiency of 16.72% and negligible hysteresis, Adv. Energy Mater. 10 (2020), https://doi.org/10.1002/aenm.202000694.

[97] H. Lai, D. Lu, Z. Xu, N. Zheng, Z. Xie, Y. Liu, Organic-salt-assisted crystal growth and orientation of quasi-2D Ruddlesden-popper perovskites for solar cells with efficiency over 19, Adv. Mater. 32 (2020) e2001470, https://doi.org/10.1002/adma.202001470.

[98] J. Liang, Z. Zhang, Y. Huang, Q. Xue, Y. Zheng, X. Wu, C. Tian, Y. Zhang, Y. Wang, Z. Chen, C.C. Chen, Volatile 2D Ruddlesden-popper perovskite: a gift for

α-Formamidinium lead triiodide solar cells, Adv. Funct. Mater. 32 (2022), https://doi.org/10.1002/adfm.202207177.

[99] Y. Qin, H. Zhong, J.J. Intemann, S. Leng, M. Cui, C. Qin, M. Xiong, F. Liu, A.K. Y. Jen, K. Yao, Coordination engineering of single-crystal precursor for phase control in Ruddlesden–popper perovskite solar cells, Adv. Energy Mater. 10 (2020), https://doi.org/10.1002/aenm.201904050.

[100] A.A. Sutanto, N. Drigo, V.I.E. Queloz, I. Garcia-Benito, A.R. Kirmani, L.J. Richter, P.A. Schouwink, K.T. Cho, S. Paek, M.K. Nazeeruddin, G. Grancini, Dynamical evolution of the 2D/3D interface: a hidden driver behind perovskite solar cell instability, J. Mater. Chem. A. 8 (2020) 2343–2348, https://doi.org/10.1039/c9ta12489f.

[101] H. Yu, L. Yan, Y. He, H. Meng, W. Huang, An unusual photoconductive property of polyiodide and enhancement by Catenating with 3-thiophenemethylamine salt, Chem. Commun. (Camb) 53 (2016) 432–435, https://doi.org/10.1039/c6cc08595d.

[102] Y. Zheng, S.C. Chen, Y. Ma, Q. Zheng, Furfurylammonium as a spacer for efficient 2D Ruddlesden–popper perovskite solar cells, Sol. RRL. 6 (2022), https://doi.org/10.1002/solr.202200221.

[103] B. Han, Y. Wang, C. Liu, K. Sun, M. Yang, L. Xie, S. Yang, Y. Meng, S. Lin, P. Xu, J. Li, Q. Qiu, Z. Ge, Rational design of ferroelectric 2d perovskite for improving the efficiency of flexible perovskite solar cells over 23, Angew. Chem. Int. Ed. Engl. 62 (2023) e202217526, https://doi.org/10.1002/anie.202217526.

[104] J. Li, K. Yan, J. Chen, Y. Zhang, W. Yang, X. Lian, G. Wu, H. Chen, Hydrogen bond enables highly efficient and stable two-dimensional perovskite solar cells based on 4-pyridine-ethylamine, Org. Electron. 67 (2019) 122–127, https://doi.org/10.1016/j.orgel.2019.01.017.

[105] Y. Li, J. Wu, Y. Zhang, L. Zhang, X. Zhou, B. Hu, Z. Jiang, J. Zeng, D. Wang, Y. Liu, S. Chen, Z. Liu, C. Liu, X. Wang, B. Xu, Whether organic spacer cations induced 2D/3D or quasi-2D/3D mixed dimensional perovskites? Chem. Eng. J. 450 (2022) https://doi.org/10.1016/j.cej.2022.137887.

[106] Y. Li, G. Zheng, C. Lin, J. Lin, Synthesis, structure and optical properties of different dimensional organic–inorganic perovskites, Solid. State Sci. 9 (2007) 855–861, https://doi.org/10.1016/j.solidstatesciences.2007.06.011.

[107] B. Fan, F. Lin, X. Wu, Z. Zhu, A.K. Jen, Selenium-containing organic photovoltaic materials, Acc. Chem. Res. 54 (2021) 3906–3916, https://doi.org/10.1021/acs.accounts.1c00443.

[108] L.A. Illicachi, J. Urieta-Mora, A. Momblona, A. Molina-Ontoria, J. Calbo, J. Arago, B. Insuasty, A. Ortiz, E. Orti, N. Martin, M.K. Nazeeruddin, Selenophene-based hole-transporting materials for perovskite solar cells, Chempluschem. 86 (2021) 1006–1013, https://doi.org/10.1002/cplu.202100208.

[109] J. Hu, I.W.H. Oswald, S.J. Stuard, M.M. Nahid, N. Zhou, O.F. Williams, Z. Guo, L. Yan, H. Hu, Z. Chen, X. Xiao, Y. Lin, Z. Yang, J. Huang, A.M. Moran, H. Ade, J. R. Neilson, W. You, Synthetic control over orientational degeneracy of spacer cations enhances solar cell efficiency in two-dimensional perovskites, Nat. Commun. 10 (2019) 1276, https://doi.org/10.1038/s41467-019-08980-x.

[110] L. Wang, Q. Zhou, Z. Zhang, W. Li, X. Wang, Q. Tian, X. Yu, T. Sun, J. Wu, B. Zhang, P. Gao, A guide to use fluorinated aromatic bulky cations for stable and high-performance 2D/3D perovskite solar cells: the more fluorination the better? J. Energy Chem. 64 (2022) 179–189, https://doi.org/10.1016/j.jechem.2021.04.063.

[111] W. Fu, H. Liu, X. Shi, L. Zuo, X. Li, A.K.Y. Jen, Tailoring the functionality of organic spacer cations for efficient and stable quasi-2D perovskite solar cells, Adv. Funct. Mater. 29 (2019), https://doi.org/10.1002/adfm.201900221.

[112] J. Hu, I.W.H. Oswald, H. Hu, S.J. Stuard, M.M. Nahid, L. Yan, Z. Chen, H. Ade, J. R. Neilson, W. You, Aryl-perfluoroaryl interaction in two-dimensional organic–inorganic hybrid perovskites boosts stability and photovoltaic efficiency, ACS Mater. Lett. 1 (2019) 171–176, https://doi.org/10.1021/acsmaterialslett.9b00102.

[113] S. Paek, C. Roldan-Carmona, K.T. Cho, M. Franckevicius, H. Kim, H. Kanda, N. Drigo, K.H. Lin, M. Pei, R. Gegevicius, H.J. Yun, H. Yang, P.A. Schouwink, C. Corminboeuf, A.M. Asiri, M.K. Nazeeruddin, Molecular design and operational stability: toward Stable 3D/2D perovskite interlayers, Adv. Sci. (Weinh) 7 (2020) 2001014, https://doi.org/10.1002/advs.202001014.

[114] J.V. Passarelli, D.J. Fairfield, N.A. Sather, M.P. Hendricks, H. Sai, C.L. Stern, S. I. Stupp, Enhanced out-of-plane conductivity and photovoltaic performance in n = 1 layered perovskites through organic cation design, J. Am. Chem. Soc. 140 (2018) 7313–7323, https://doi.org/10.1021/jacs.8b03659.

[115] H. Yao, Z. Li, C. Shi, Y. Xu, Q. Wang, Z. Li, G. Peng, Y. Lei, H. Wang, Z. Ci, Z. Jin, A novel multiple-ring aromatic spacer based 2D ruddlesden–popper CsPbI3solar cell with record efficiency beyond 16%, Adv. Funct. Mater. 32 (2022) https://doi.org/10.1002/adfm.202205029.

[116] B.E. Cohen, Y. Li, Q. Meng, L. Etgar, Dion-jacobson two-dimensional perovskite solar cells based on benzene dimethanammonium cation, Nano Lett. 19 (2019) 2588–2597, https://doi.org/10.1021/acs.nanolett.9b00387.

[117] R. Zhao, R.P. Sabatini, T. Zhu, S. Wang, A. Morteza Najjarian, A. Johnston, A. J. Lough, S. Hoogland, E.H. Sargent, D.S. Seferos, Rigid conjugated diamine templates for stable dion-jacobson-type two-dimensional perovskites, J. Am. Chem. Soc. 143 (2021) 19901–19908, https://doi.org/10.1021/jacs.1c09515.